Nonlinear modelling of arrays of submerged wave energy converters

David, Daniel Raj; Wolgamot, Hugh; Kurniawan, Adi; Hansen, Jeff; Rijnsdorp, Dirk

DOI
10.1016/j.oceaneng.2024.118669

Publication date
2024

Document Version
Final published version

Published in
Ocean Engineering

Citation (APA)
David, D. R., Wolgamot, H., Kurniawan, A., Hansen, J., & Rijnsdorp, D. (2024). Nonlinear modelling of arrays of submerged wave energy converters. *Ocean Engineering*, *310*, Article 118669. https://doi.org/10.1016/j.oceaneng.2024.118669

Ocean Engineering 310 (2024) 118669

Contents lists available at ScienceDirect

Ocean Engineering

journal homepage: www.elsevier.com/locate/oceaneng

Research paper

Nonlinear modelling of arrays of submerged wave energy converters

Daniel Raj David [a,b,c,*], Hugh Wolgamot [a,b,c], Adi Kurniawan [a,b], Jeff Hansen [b,c,d], Dirk Rijnsdorp [e]

[a] Oceans Graduate School, The University of Western Australia, Australia
[b] Marine Energy Research Australia, The University of Western Australia, Australia
[c] UWA Oceans Institute, The University of Western Australia, Australia
[d] School of Earth Sciences, The University of Western Australia, Australia
[e] Delft University of Technology, Delft, Netherlands

ARTICLE INFO

Keywords:
Wave energy converters
SWASH
Array interactions
Wave farm
Wave power
Optimization

ABSTRACT

Studies of arrays of wave energy converters (WECs) with respect to power absorption and array interactions are often performed using linear models. However, nonlinear effects can be important and may change power estimates and optimal array designs. In this study, we have compared linear predictions of the behaviour of a shallowly submerged, buoyant point absorber with predictions from the nonlinear model SWASH with a WEC incorporated (WEC-SWASH). The latter was first comprehensively validated against 1:20 Froude scaled measured data from physical experiments. WEC-SWASH predictions of body motions and mean power absorption were generally in good agreement with measurements (absolute bias within 25%), although some discrepancies were observed in the body motions, especially when the device exhibited motion instabilities. The validated WEC-SWASH model was then compared with a linear frequency-domain model, as the latter is well-known and widely used because of its computational efficiency. Model comparisons were carried out for both an isolated WEC and small arrays (up to 5 devices). The mean power estimates from the linear model and WEC-SWASH for two representative wave farms showed good agreement for mild waves, with a difference of less than 5%. However, for larger waves, the disagreement increased to about 75 to 85% between the models (for the two wave farms tested). We found that array interactions for these arrays depend on wave amplitude and not just wave frequency. Furthermore, we discovered that the power take-off coefficients optimized using the linear model were not the optimum coefficients for the nonlinear model (WEC-SWASH).

1. Introduction

To generate substantial power, wave energy converters (WECs) will need to be deployed in arrays (wave farms). WECs deployed in arrays will interact with each other through their radiated and scattered wave fields. These interactions, known as the "park effect" (Babarit, 2013), can influence the overall power production of the farm. Ideally wave farm layouts aim to utilize the constructive interactions to increase power production but in most realistic settings arrays are optimized to minimize destructive interactions (e.g., McIver, 1994; Penalba et al., 2017c).

To study WEC array interactions and power production, efficient and accurate computational models accounting for the relevant physics are essential. Although reduced-scale physical modelling provides an accurate representation of the full-scale physical effects in many cases, physical modelling studies are costly and limit the number and size of arrays that can be examined. Modelling arrays in wave basins is limited by the physical size of the basin, entailing scale effects and reflected waves. As such, the majority of existing array studies have used numerical modelling (e.g., Göteman et al., 2020; Stavropoulou et al., 2023), while there are fewer laboratory studies (e.g., Faedo et al., 2023; Özkan-Haller et al., 2017; Stratigaki et al., 2014). Commonly used numerical models include linear potential flow solvers using the boundary element method (BEM), e.g., WAMIT, NEMOH and ANSYS AQWA. BEM solvers are primarily used to study the power absorption characteristics of arrays, including WEC interactions, but most studies are limited to linear wave-structure interactions (e.g., Li and Yu, 2012; Göteman et al., 2020). Linear wave theory assumes that waves are of small amplitude (compared to wavelength and water depth) and the associated body motions of WECs/structures are small with nonlinearities in the wave-WEC interactions (e.g., higher harmonics, flow separation and slamming) not accounted for. For a more accurate representation of WECs and response predictions (especially due to extreme waves), Computational Fluid Dynamics (CFD) models have been used. As CFD models are based on the fundamental conservation of

* Corresponding author at: Oceans Graduate School, The University of Western Australia, Australia.
E-mail address: danielraj.david@uwa.edu.au (D.R. David).

https://doi.org/10.1016/j.oceaneng.2024.118669
Received 4 April 2024; Received in revised form 1 July 2024; Accepted 3 July 2024
Available online 14 July 2024

mass and momentum balance equations, they more accurately capture wave-WEC interactions. However, they are computationally demanding and typically require supercomputing facilities. Some notable studies have applied CFD codes to simulate WEC arrays (e.g., Agamloh et al., 2008; Westphalen, 2011); however, they limited their application to a small number of WECs with relatively small spatial and temporal scales. Due to their computational demands, CFD models are not suited to resolve the dynamics of large WEC farms, at least at the present state of the art. Although computational power is increasing, it is beneficial to utilize methods that are quicker in capturing nonlinear wave-WEC interactions.

Reducing computational time without undermining the accuracy of WEC responses and thereby power absorption has been a challenge. Existing models and nonlinear approaches to capture the nonlinear WEC responses for various isolated WECs have been reviewed by Penalba et al. (2017a) and Wolgamot and Fitzgerald (2015). Some studies employ partially nonlinear formulations as not all nonlinear effects are equally important in contributing to the body motions (Davidson and Costello, 2020). While it is useful to have models that can accurately predict the nonlinear responses of an isolated WEC, it is also crucial to extend these models to arrays. When considering arrays of WECs, the computational expense drastically increases (Folley, 2016). A few studies have adopted partially nonlinear approaches by considering the nonlinear Froude–Krylov forces (e.g., Penalba et al., 2017b; Davidson and Costello, 2020; Giorgi and Ringwood, 2017) and nonlinear weak-scatterer approach (e.g., Zhang et al., 2021). However, the representation of radiated wave fields through which WEC array interactions occur has received much less attention in such models, such that extension to large arrays remains an area of research. Other approaches include Boussinesq models (Venugopal and Smith, 2007) which, however, are not directly applicable to floating WECs.

A number of existing studies used linear wave-WEC interactions to predict power absorption by arrays with application to array optimization (refer to Göteman et al., 2020 for a detailed review of existing approaches for wave farm optimization). As wave farm optimization generally requires the evaluation of many arrays, linear potential flow theory is the only plausible method currently suitable. Although linear potential flow-based approaches provide acceptable levels of accuracy in some situations, studies have also shown that linear potential flow-based models were insufficient to capture nonlinear wave-WEC interactions (Giorgi and Ringwood, 2017; Rafiee and Fiévez, 2015; Schubert et al., 2020) which are important for shallowly submerged devices. For shallowly submerged devices (similar to Fig. 1), nonlinear responses/motions arise even when the waves are rather small (e.g., due to nonlinear hydrodynamic effects McCauley et al., 2023). This implies that power absorption estimates from linear theory approaches may be inaccurate. Furthermore, it is widely known that power absorption (and hence array optimization) can be improved significantly through a suitable control strategy that tunes the power take-off (PTO) to the incoming waves. The choice of the optimal PTO parameters will be influenced by nonlinear wave-WEC interactions. In this study, this is demonstrated through a simplified approach using a linearized spring and damper to represent the (passive) PTO. We note several control strategies exist for nonlinear modelling, see also Karthikeyan et al. (2019), O'Sullivan and Lightbody (2017), Scruggs and Lao (2019). For a more detailed review of different control strategies, and their advantages and limitations, readers are referred to Faedo et al. (2019, 2017), Fusco et al. (2010), Hals et al. (2010) and Ringwood et al. (2014).

In this work, we aim to understand the differences in power absorption estimates obtained using linear and nonlinear hydrodynamic models for a submerged three-tethered point absorber WEC, both when operating singly as well as in arrays. For the nonlinear model, we used the open-source non-hydrostatic model SWASH (Zijlema et al., 2011), modified (Rijnsdorp et al., 2018) to include single or multiple submerged three-tethered WECs, hereafter referred to as WEC-SWASH. WEC-SWASH is computationally attractive relative to most CFD models, with the use of coarse vertical layers reducing computational demand (especially for larger wave farms with large spatial and temporal scales) while accounting for important nonlinear effects. Rijnsdorp et al. (2018) validated the WEC-SWASH model by comparing predictions with linear potential flow theory, for very small incident waves; and laboratory and numerical experiments with a submerged pontoon (fixed position) and a submerged floating breakwater (similar to a submerged point absorber), for nonlinear wave conditions. The model predictions were in good agreement in terms of wave-induced device motions, mooring line forces and wave evolution. Due to the lack of measured laboratory data with the submerged WEC at the time of implementation, the WEC-incorporated SWASH model was not fully validated with laboratory or other measurements for this WEC. With the recent availability of laboratory measurements (Orszaghova et al., 2020), we pursue further validation of WEC-SWASH. With the validated model we are then able to address the differences in power absorption estimates between WEC-SWASH and the linear frequency-domain model. The paper is therefore laid out as follows: Section 2 introduces the numerical models used in this study, i.e., the nonlinear WEC-SWASH model and the linear model which describes the frequency-domain transfer functions from incident wave amplitude to linear rigid body motions. In Section 3, the experiment and numerical model for a single WEC are described before results are compared for validation. Section 4 compares WEC-SWASH and the linear model for both isolated device and arrays. Finally, in Section 5, the main findings of the study are summarized in the discussion and conclusion, along with the limitations.

2. Methodology

2.1. Numerical model - SWASH

WEC-SWASH (Rijnsdorp et al., 2018) is the nonlinear numerical model used in this study. It is based on the Reynolds-Averaged Navier–Stokes equations for an incompressible fluid of constant density. The fluid domain is confined between the seabed $z = -d(x, y)$ at the bottom boundary and the free-surface $z = \zeta(x, y, t)$. The WEC (submerged) is bounded by the top and bottom at $z = -S_t(x, y, t)$ and $z = -S_b(x, y, t)$, respectively. Here, t is time and $\langle x, y, z\rangle$ denote Cartesian coordinates. The governing equations using the Einstein summation convention read

$$\frac{\partial u_j}{\partial x_j} = 0\,, \tag{1}$$

$$\frac{\partial u_i}{\partial t} + \frac{\partial u_i u_j}{\partial x_j} + \frac{\partial p}{\partial x_j} + g_i = \frac{\partial \tau_{ij}}{\partial x_j}\,, \tag{2}$$

where $i, j \in \langle 1, 2, 3\rangle$, with $\langle x_1, x_2, x_3\rangle = \langle x, y, z\rangle$, g_i represents the contribution of the gravitational acceleration $\langle 0, 0, g\rangle$ ($g = 9.806$ m/s^2), u_i is the velocity component of $\vec{u}$ in the direction x_i, and τ_{ij} represents the turbulent stress (which is estimated based on the eddy viscosity approximation). The total normalized pressure p is given as $p = g(\zeta - z) + p_{nh}$; in which the first and second terms represent the hydrostatic and non-hydrostatic pressure. WEC-SWASH accounts for the fully nonlinear kinematic boundary condition at the free surface and solves at most second-order spatial derivatives, while the applied finite difference approximations are at most second-order accurate in both time and space. Surface tension is neglected, as are tangential stresses at the WEC surface. Furthermore, in WEC-SWASH, the free surface is a single-valued function of the horizontal coordinates and the Keller-Box scheme (Lam and Simpson, 1976; Stelling and Zijlema, 2003) is used to resolve the dispersive properties. This led to a considerable decrease in computational time for WEC-SWASH when compared to RANS-based CFD models, especially combined with the use of coarse vertical layers (Rijnsdorp et al., 2018). In WEC-SWASH, the vertical motions are directly represented in the grid, as the layers follow the

top and bottom surfaces of the WEC, while the horizontal and rotational motions are linearized, i.e., there is no change in the grid due to these motions. The WEC motions are determined based on Newton's Second Law using the linearized rigid body equations,

$$\mathbf{F} = m\frac{d^2\mathbf{X}}{dt^2}\,, \tag{3}$$

$$\mathbf{M} = \mathbf{I}\frac{d^2\boldsymbol{\Theta}}{dt^2}\,, \tag{4}$$

in which $\mathbf{F} = (F_x, F_y, F_z)$ and $\mathbf{M} = (M_x, M_y, M_z)$ are the external forces and moments acting on the body, m is the mass (= 248 kg in model scale), refer Table 1 for more details, and $\mathbf{I} = \mathrm{diag}(I_x, I_y, I_z)$ is the moment of inertia matrix of the structure with respect to the centre of gravity. $\mathbf{X}$ and $\boldsymbol{\Theta}$ represent the translational and rotational motions of the body with respect to its centre of gravity. The forces and moments induced by the tethers and PTOs (that depend on the tether configuration) are given as

$$\mathbf{F}_i = -\mathbf{n}_i\left(C + K_{pto}l_i + B_{pto}\frac{\partial l_i}{\partial t}\right). \tag{5}$$

where $\mathbf{n}_i$ is the unit vector along tether i, $i \in \langle 1,2,3\rangle$ representing three tethers, C is the tether pretension to counteract the net buoyancy force, l_i is the tether extension, and K_{pto} and B_{pto} represent the PTO's stiffness and damping coefficients, respectively. The PTO acts as a linear spring-damper. For more details on WEC implementation, numerical interpretation, and associated assumptions, readers are referred to Rijnsdorp et al. (2018).

2.2. Linear model

The linear model used in this work is a set of frequency-domain transfer functions from incident wave amplitude to linear rigid body motions. By assuming harmonic response, the linear system of equations in the frequency domain can be written as (Falnes, 2002)

$$\hat{\boldsymbol{F}}_e(\omega) = \left[i\omega(\boldsymbol{M} + \boldsymbol{A}_m) + (\boldsymbol{B} + \boldsymbol{B}_{pto}) + \frac{\boldsymbol{K}_{pto}}{i\omega}\right]\hat{\boldsymbol{U}}(\omega)\,, \tag{6}$$

where $\hat{\boldsymbol{U}}$ is the vector of complex velocity amplitudes, $\hat{\boldsymbol{F}}_e$ is the vector of complex excitation forces (including the array interactions), $\boldsymbol{A}_m(\omega)$ and $\boldsymbol{B}(\omega)$ are the frequency-dependent added mass and radiation damping matrices, $\boldsymbol{M}$ is the mass matrix, $\boldsymbol{K}_{pto}$ and $\boldsymbol{B}_{pto}$ are the linearized PTO stiffness and damping coefficient matrices, for more details, refer to Orszaghova et al. (2020). The PTO coefficients are assumed identical for all three PTOs per WEC and in this paper PTO coefficients for the linear model are chosen by optimization - see Section 4.1. The total mean power (P) produced by an isolated WEC (or an array of N WECs) oscillating in six degrees of freedom is calculated using (Budal, 1977; Falnes and Budal, 1982; Thomas and Evans, 1981)

$$P = \frac{1}{4}\left[\hat{\boldsymbol{U}}^*\hat{\boldsymbol{F}}_e + \hat{\boldsymbol{F}}_e^*\hat{\boldsymbol{U}}\right] - \frac{1}{2}\hat{\boldsymbol{U}}^*\boldsymbol{B}\hat{\boldsymbol{U}}\,. \tag{7}$$

where the asterisk denotes the complex conjugate transpose.

3. WEC-SWASH validation

3.1. Description of the experimental setup and wave conditions

To validate WEC-SWASH we used 1:20 Froude model-scale data from the experimental campaign jointly carried out by Carnegie Clean Energy and the University of Western Australia in the Ocean Basin at the Coastal, Ocean and Sediment Transport Laboratory (COAST Lab), University of Plymouth, UK. The wave basin is 15 m wide and 30 m long. The device considered in this study is a shallowly submerged cylindrical device similar to Carnegie's CETO-6 device (see Fig. 1). The WEC model was deployed in the centre of the basin (see Fig. 2). The device was moored to the floor by three taut tethers at an angle of 40° (relative to vertical). The tether attachment point at the buoy was fixed

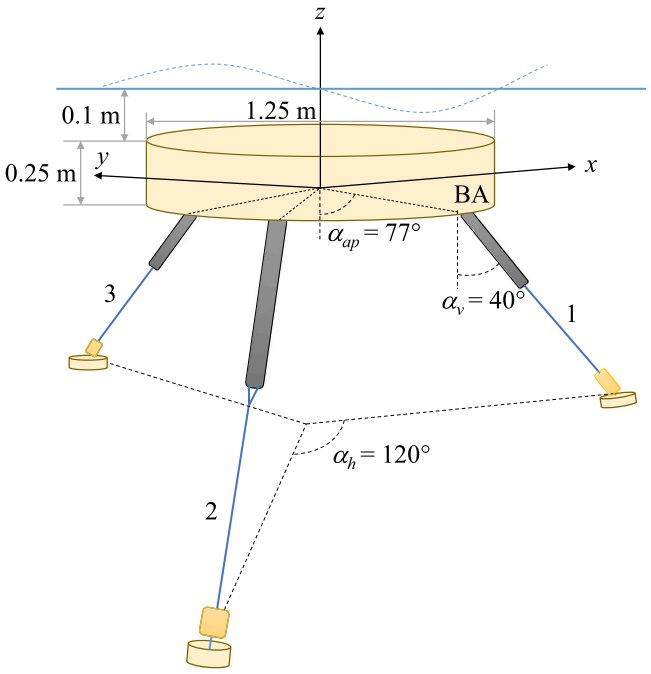

Fig. 1. Scaled down submerged three-tethered CETO-6 WEC design after Carnegie Clean Energy.

Table 1
Adopted device configurations in the 1:20 Froude scale experimental study.

Parameter	Model scale (1:20)	Full scale (1:1)
WEC diameter	1.25 m	25 m
WEC thickness	0.25 m	5 m
WEC submergence	0.1 m	2 m
Water depth at model	1.5 m	30 m
Mass	248 kg	1,984,000 kg
Tether angle, α_v	40°	40°
Attachment point angle, α_{ap}	77°	77°
Power Take-off (PTO) pre-tension, C	560 N	4,480,000 N

Table 2
Wave conditions. H = wave height, T = wave period, H_s = significant wave height, T_p = peak wave period, L = wavelength and L_p = peak wavelength.

Wave Type	Parameter	Model scale (Range)	Full scale (Range)
Regular Waves			
	H (m)	0.03–0.15	0.6–3
	T (s)	1.01–2.82	4.5–12.6
	$\frac{H}{L}$	0.004–0.063	0.004–0.063
Irregular Waves			
	H_s (m)	0.1–0.25	2–5
	T_p (s)	1.79–4.02	8–18
	$\frac{H_s}{L_p}$	0.003–0.05	0.003–0.05

at an angle of 77° (relative to vertical) from the centroid of the buoy to the attachment point. The details of the device parameters and the range of wave conditions (both regular and irregular) adopted in the experimental study are shown in Table 1 and Table 2, respectively.

The buoy was moored using equal-length tethers with one tether (L1) pointing in the wave propagation direction (i.e., downwave) and the other two (L2 and L3) pointing 120 degrees apart in the opposite direction. To understand the wave evolution (especially relevant as the waves were generated in water 3.5 m deep and travelled up a ramp to the model in 1.5 m of water), 12 wave gauges were installed at different locations (see Fig. 2). An absorbing (convex) beach was used to minimize the incident wave reflection at the absorber end. The WEC was equipped with three PTOs represented with a rope, winch and pulley system similar to that in Peckolt et al. (2015). The

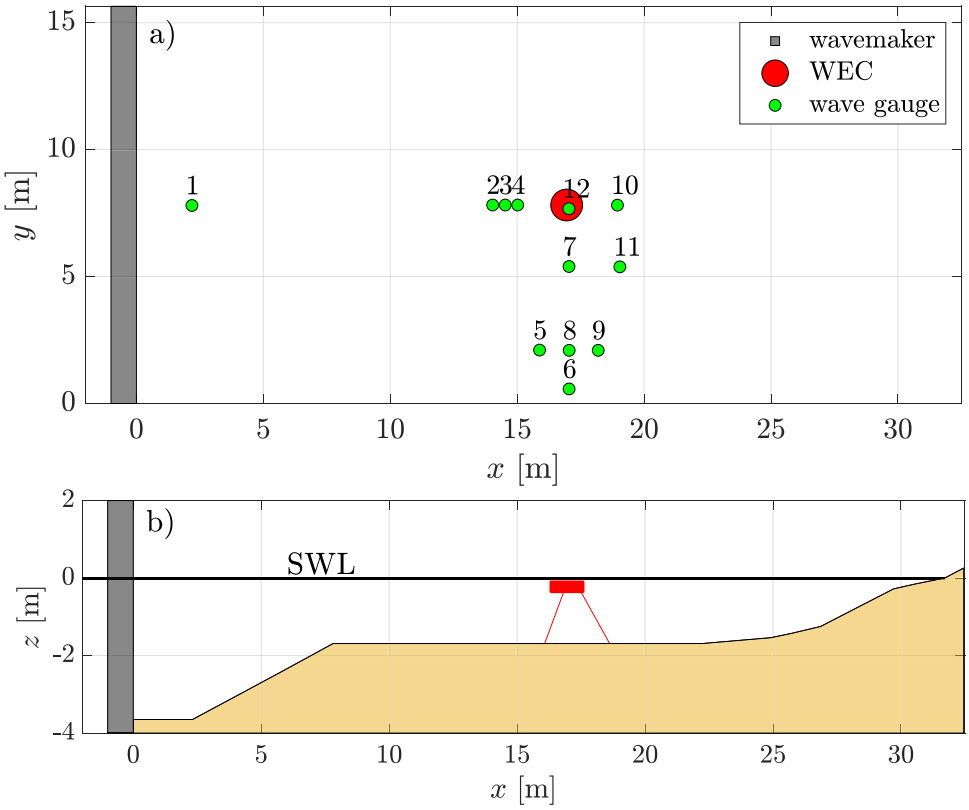

Fig. 2. Experimental setup. (a) Plan view of the wave tank with locations of the wave gauges, wavemaker and the WEC; (b) Cross-section of the tank with bottom profiles. SWL = Still Water Level.

PTO coefficients, namely the stiffness, K_{pto} (N m^{-1}) and damping, B_{pto} (Ns m^{-1}) coefficients were varied for different wave conditions. A state-of-the-art motion capture system was used to track and measure the buoy's instantaneous position in all 6 degrees of freedom (DOF). For more details on the experimental procedure, readers are referred to Orszaghova et al. (2020).

The experimental setup (Fig. 2) was simulated in SWASH (in model scale) with a cyclic boundary condition at the lateral boundaries and a sponge layer at the wave absorber end to absorb the outgoing waves. The length of the sponge layer was two wavelengths in all simulations. The PTO coefficients (K_{pto} ranging between 400–4200 N m^{-1} and B_{pto} between 1130–5000 Ns m^{-1}) were set to the same combination of values as used in the experimental runs for various wave conditions. The wave boundary was forced by the target amplitude and phase for regular waves, whereas, for irregular waves, we first extracted the Fourier components measured from wave gauge 1 in front of the wavemaker and reconstructed the waves at the wave paddle to impose in SWASH. A constant rectilinear grid was considered in the SWASH domain with Δx and Δy corresponding to 12–28 points per buoy diameter and about 80 points per wavelength. The chosen grid resolution was based on an initial sensitivity study carried out by varying the number of points per buoy diameter from 10 to 50 and by comparing the simulated body motions with the measurements for 2 representative wave conditions (i.e., $H = 0.05$ m, $T = 1.067$ s and $H_s = 0.1$ m and $T_p = 1.79$ s). Furthermore, in SWASH, a minimum of three vertical layers ($V_n = 3$) is needed to study submerged cylinders (Rijnsdorp et al., 2018) such that one layer is fixed below the cylinder, one layer at the cylinder, and one at the free surface. Similar to the grid resolution sensitivity study, we carried out a vertical resolution sensitivity study with the same representative conditions and fixed the number of vertical layers as 5. However, it was found that the difference between 3 and 5 vertical layers was trivial. For the 5 layers, 2 layers were above the cylinder, one layer at the cylinder, and 2 were below the cylinder.

3.2. Regular wave comparison – an illustrative example

Fig. 3 shows the time histories and power spectral densities (PSDs) from SWASH and the experiment for a representative wave condition $H = 0.05$ m and $T = 1.067$ s. The number of waves (about 220) simulated in SWASH is the same as in the experiment. SWASH took about 6.5 h to run on 96 CPUs. We used Welch's method (Welch, 1967) with 50% overlapping windows to compute the PSDs. The incident wave (η_{w1}, wave gauge 1 in Fig. 3a) comparison shows that the WEC-SWASH predicted amplitude is about 8% smaller than the measured (Fig. 3a). Although we considered all six degrees of freedom (dof), the sway, roll, and yaw motions were not excited in this wave condition. Therefore, only the instantaneous buoy motions and PSDs in the surge (X, S_X), heave (Z, S_Z), and pitch (θ_y, S_y) dof are shown in Fig. 3c-h respectively. For illustrative purposes, the time histories are normalized by the incident wave height (H), except for pitch motion. The comparison revealed a good agreement for surge and pitch (Fig. 3c, d, and g, h); however, SWASH predictions are slightly larger than the experiments (2% and 6% for surge and pitch respectively). Furthermore, SWASH predictions for first harmonic heave are 24% lower than that measured for this condition. During the experimental run, we observed some drift in the mean vertical position (Fig. 3e). Although the incoming waves are largely linear, the device exhibits a nonlinear response, as discussed in McCauley et al. (2018, 2023), for example. SWASH captured this nonlinear effect; however, the magnitude of this mean drift and the wave-frequency motions were slightly underpredicted (by about 15%). To attempt to resolve this mismatch in heave responses, we carried out additional simulations by increasing the vertical resolution up to 10 layers. This improved the heave predictions, but the surge and pitch responses were overpredicted compared to the case with five vertical layers. We did not investigate the cause of the slight discrepancy in the mean position as we focus mainly on irregular waves in the remainder of the paper.

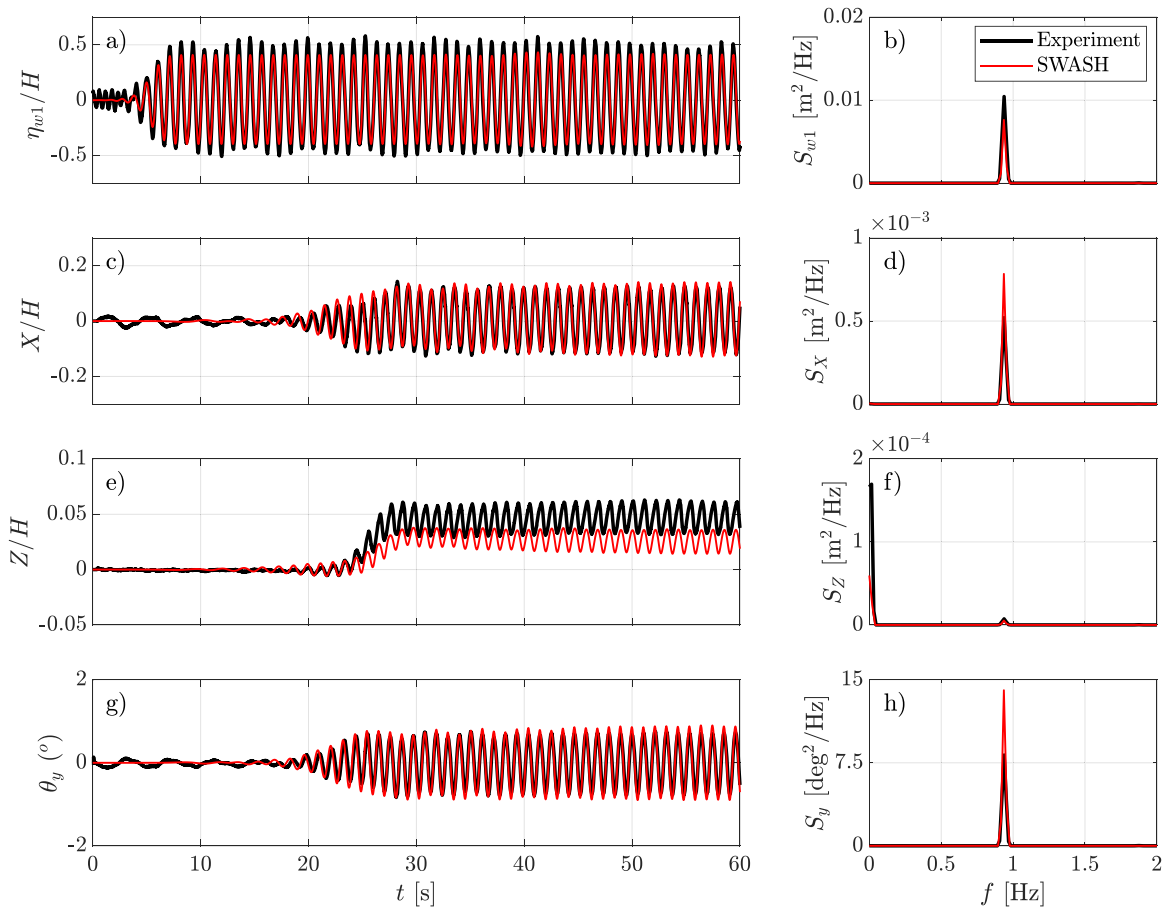

Fig. 3. Comparison of SWASH predicted and experimentally measured time histories and power spectral densities (PSDs) subject to $H = 0.05$ m and $T = 1.067$ s. Panels (a) and (b) show the normalized (by incident wave height) time history and PSD of the incident wave. Panels (c), (e), and (g) show the time histories of surge, heave and pitch motions with their PSDs in (d), (f), and (h), respectively.

3.3. Irregular wave comparison – an illustrative example

In comparing the model to the irregular wave tests, as for regular waves, we first focused our comparisons on relatively mild wave conditions. Fig. 4 shows a comparison of time histories and PSDs for $H_s = 0.1$ m, $T_p = 1.79$ s, for a run of about 540 s; however, for clarity and to highlight the discrepancies, the time window is fixed as one minute (100 s to 160 s) and is shown in Fig. 4. An overall comparison shows excellent agreement in terms of the time histories; however, the PSDs reveal some discrepancies in magnitude for the low-frequency peaks (Fig. 4d, h). Therefore, for the body motions, time signals corresponding to the low-frequency peaks are band-pass filtered and shown separately (Fig. 4c-h). WEC-SWASH captures low-frequency surge/pitch motions (which would not be captured by a linear model), but which are nevertheless underpredicted in comparison to the measured responses e.g., Fig. 4d, h. These large motions in surge/pitch could be associated with instability (Fig. 4d, h) as a result of coupled surge-pitch resonance and are discussed in detail in 'Response spectra comparison' section. Notably, these low-frequency motions did not feed back to significant changes in the prediction of wave-frequency heave motion and did not significantly influence the power absorption. This is due to the stronger coupling of the PTO with heave motion compared to surge/pitch. It is important to highlight here that the tether and PTO systems are integrated, and therefore all six modes of motion are coupled (Orszaghova et al., 2020). However, due to the strong and weak coupling of different modes of motions with the PTOs, not all motions contribute to power absorption equally.

3.4. Tether extension

The power absorption in CETO-6 and similar taut-moored WECs is related to the rate of change of the tether lengths. The tether extensions, namely l_1, l_2, and l_3 corresponding to tethers 1, 2, and 3, are calculated from the buoy motions based on the method given in Orszaghova et al. (2020):

$$l_1 \approx Z\cos(\alpha_v) - X\sin(\alpha_v) + \theta_y r\sin(\alpha_v - \alpha_{ap}) , \tag{8}$$

$$l_2 \approx Z\cos(\alpha_v) + \frac{1}{2}(X + \sqrt{3}Y)\sin(\alpha_v) - \frac{1}{2}(\theta_y - \sqrt{3}\theta_x)r\sin(\alpha_v - \alpha_{ap}) , \tag{9}$$

$$l_3 \approx Z\cos(\alpha_v) + \frac{1}{2}(X - \sqrt{3}Y)\sin(\alpha_v) - \frac{1}{2}(\theta_y + \sqrt{3}\theta_x)r\sin(\alpha_v - \alpha_{ap}) , \tag{10}$$

where r is the distance from the centre of the buoy to the attachment point, X, Y, Z represent the translational motions, and θ_x, θ_y, θ_z represent the rotational motions. α_v and α_{ap} are the angle from the sea bed to the tether attachment point and tether attachment point to the centroid (see also Fig. 1). The tether extension calculations are validated with the measured data.

Fig. 5 compares tether extensions for the same wave conditions considered in Figs. 3 and 4. Similar to Fig. 4, the tether extensions were comparable between SWASH and the experiment for irregular waves (Fig. 5d, e, f). For regular waves, as a result of the shift in the mean heave position and the mismatch observed in Fig. 3, the tether extensions revealed some discrepancies between SWASH and the experiment. Although SWASH captured this nonlinear behaviour, the magnitude of the response was not fully captured (Fig. 5b, c). Nevertheless, for some wave conditions, the device exhibits linear behaviour, and a reasonable agreement was observed.

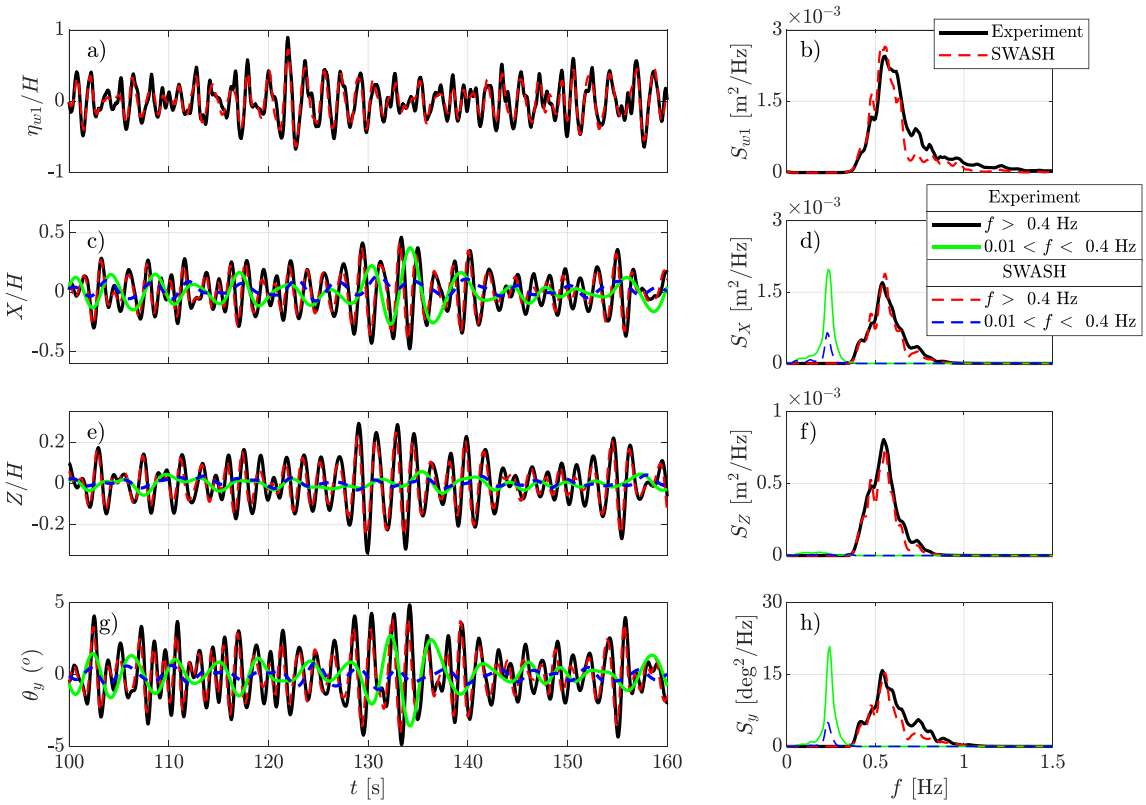

Fig. 4. Comparison of SWASH predicted and experimentally measured time histories and power spectral densities (PSDs) subjected to $H_s = 0.1$ m and $T_p = 1.79$ s. Panels (a) and (b) show the normalized time history and PSD of the incident wave. Panels (c), (e), and (g) show the time histories of surge, heave and pitch motions with their PSDs in (d), (f), and (h), respectively.

3.5. Response spectra comparison

As all modes of motion are coupled in the CETO-6 device, motion instabilities (sometimes referred to as 'parametric excitation' or 'resonance') can occur for some modes as a result of time-varying restoring stiffness. Such instabilities can affect power production (both positively or negatively) and may also be detrimental to the device's structural integrity. A number of existing studies investigated motion instabilities in different types of WECs (Giorgi and Ringwood, 2019, Kurniawan et al., 2019, Orszaghova et al., 2019, Tarrant and Meskell, 2016, Davidson et al., 2022). A recent study explained yaw (θ_z) instability for the CETO-6 type WEC (Orszaghova et al., 2020), where yaw instability has also been observed for other structures (Giorgi et al., 2020). Although investigating motion instabilities is not the major focus of this study, it is important to highlight that SWASH was able to capture some motion instabilities observed during the experiments.

Fig. 6 shows the normalized wave and normalized response spectra (PSD/max(PSD)) comparison subject to $H_s = 0.2$ m and $T_p = 2.68$ s, for which we observed yaw instability. For both experiment and SWASH, we normalized the response spectra using the max(PSD_{Exp}) obtained from the experiment. The undamped natural frequencies of each mode (including coupled modes) are calculated using the method in Orszaghova et al. (2020) with hydrodynamic coefficients obtained from McCauley et al. (2018). For the coupled surge and pitch modes, the eigenvalue problem results in more than two possible roots (i.e., $\omega^{\pm}_{n15}$), and only the natural frequencies corresponding to the frequency range of interest are shown in Fig. 6.

Although SWASH was forced with the measured incident wave, as a result of sensitivity to spatial and temporal resolution and numerical interpretation in wave generation, we observed some negligible discrepancies (Fig. 6, incident wave spectra). The SWASH predicted response follows the experimentally measured peaks with a slight difference in magnitude. The yaw and heave responses were overpredicted, and the surge and pitch responses were underpredicted. On comparing the yaw magnitude across all simulations (both regular and irregular waves), SWASH predictions are generally larger than measurements by about 4 to 46%.

3.6. Summary comparison

To summarize the comparison across all wave conditions (20 regular wave and 81 irregular wave cases were simulated of duration 300 s and 540 s respectively), we computed the dynamic response for each motion from both regular and irregular waves. For regular waves, the amplitude of the body responses from the steady-state solution are taken, whereas, for irregular waves, we computed the significant response from the zeroth spectral moments ($4\sqrt{m_0}$). Although all six degrees of freedom were considered, only surge (X), heave (Z), and pitch (θ_y) motions are compared in Fig. 7.

As some wave conditions resulted in yaw (θ_z) instabilities, we first excluded these conditions from the comparison (Fig. 7a, b). Similar to Orszaghova et al. (2020), we used a threshold of 1° standard deviation (σ_z) to categorize the θ_z instabilities. The unstable conditions (plotted in grey) are included along with the stable conditions and compared in Fig. 7c, d, respectively.

For illustrative purposes, we computed four statistical measures for the body responses: scatter index (SI), relative bias (RB), correlation coefficient (R) and linear regression slope (m). The first three measures are defined below.

$$\text{SI} = \frac{\sqrt{\frac{1}{N}\sum_{i=1}^{N}(Q_s^i - Q_e^i)^2}}{\frac{1}{N}\sum_{i=1}^{N} Q_e^i}, \tag{11}$$

$$\text{RB} = \frac{\sum_{i=1}^{N}(Q_s^i - Q_e^i)}{\sum_{i=1}^{N} Q_e^i}, \tag{12}$$

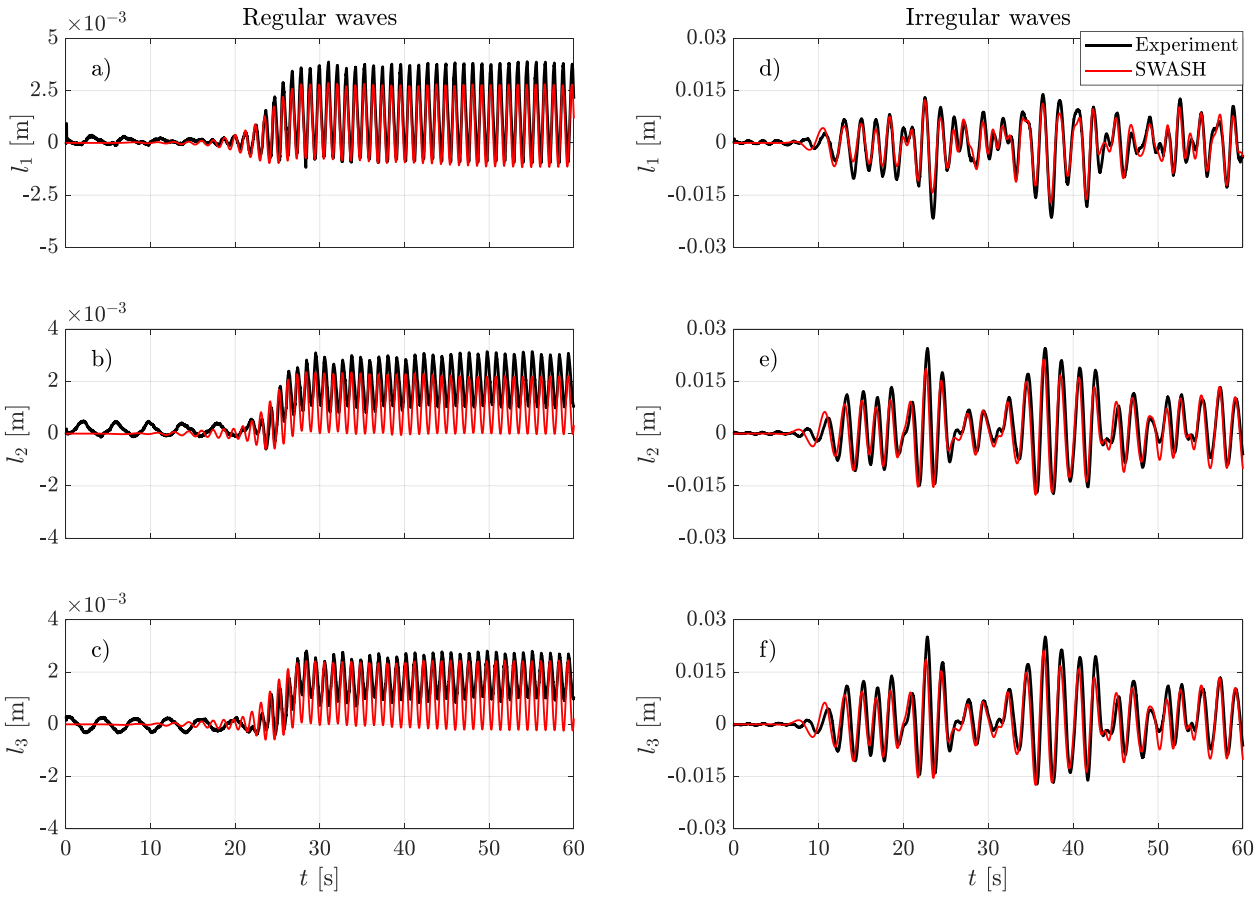

Fig. 5. Comparison of instantaneous tether extension from SWASH and experiment for both regular (H = 0.05 m and T = 1.067) and irregular (H_s = 0.1 m and T_p = 1.79 s) waves. Panels a, b, (c) - regular waves, panels d, e, (f) - irregular waves.

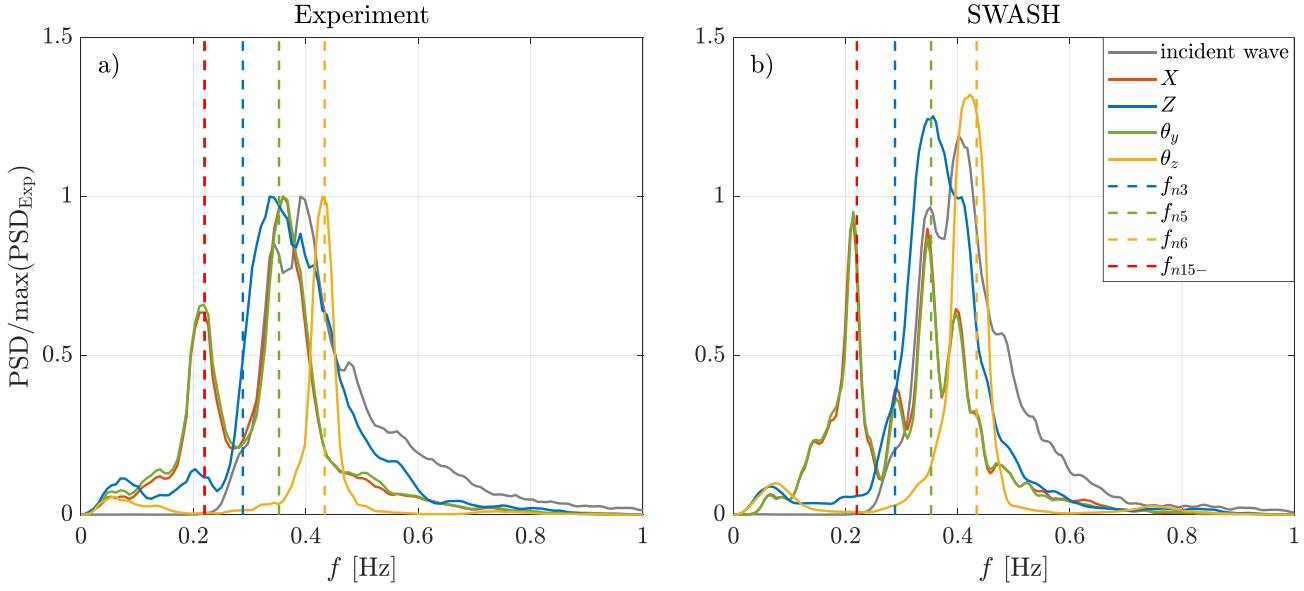

Fig. 6. Comparison of wave and WEC response spectra from the experiment (a) and SWASH (b) subject to significant wave height, H_s = 0.2 m and peak wave period of T_p = 2.68 s. The dotted lines represent the undamped natural frequencies $f_n = \omega_n/2\pi$.

$$\mathrm{R} = \frac{1}{N-1}\sum_{i=1}^{N}\left(\frac{Q_s^i - \mu_{Q_s}}{\sigma_{Q_s}}\right)\left(\frac{Q_e^i - \mu_{Q_e}}{\sigma_{Q_e}}\right), \tag{13}$$

where Q_s is the SWASH predicted parameter and Q_e is the experimentally measured parameter. μ and σ are the mean and standard deviation. The value R = 1 denotes an exact match between SWASH and experimentally measured parameters (body motions and power absorption estimation). The statistical measures are tabulated individually in Table 3 for regular and irregular waves. Overall, we found good accuracy between SWASH and experiments for both regular and

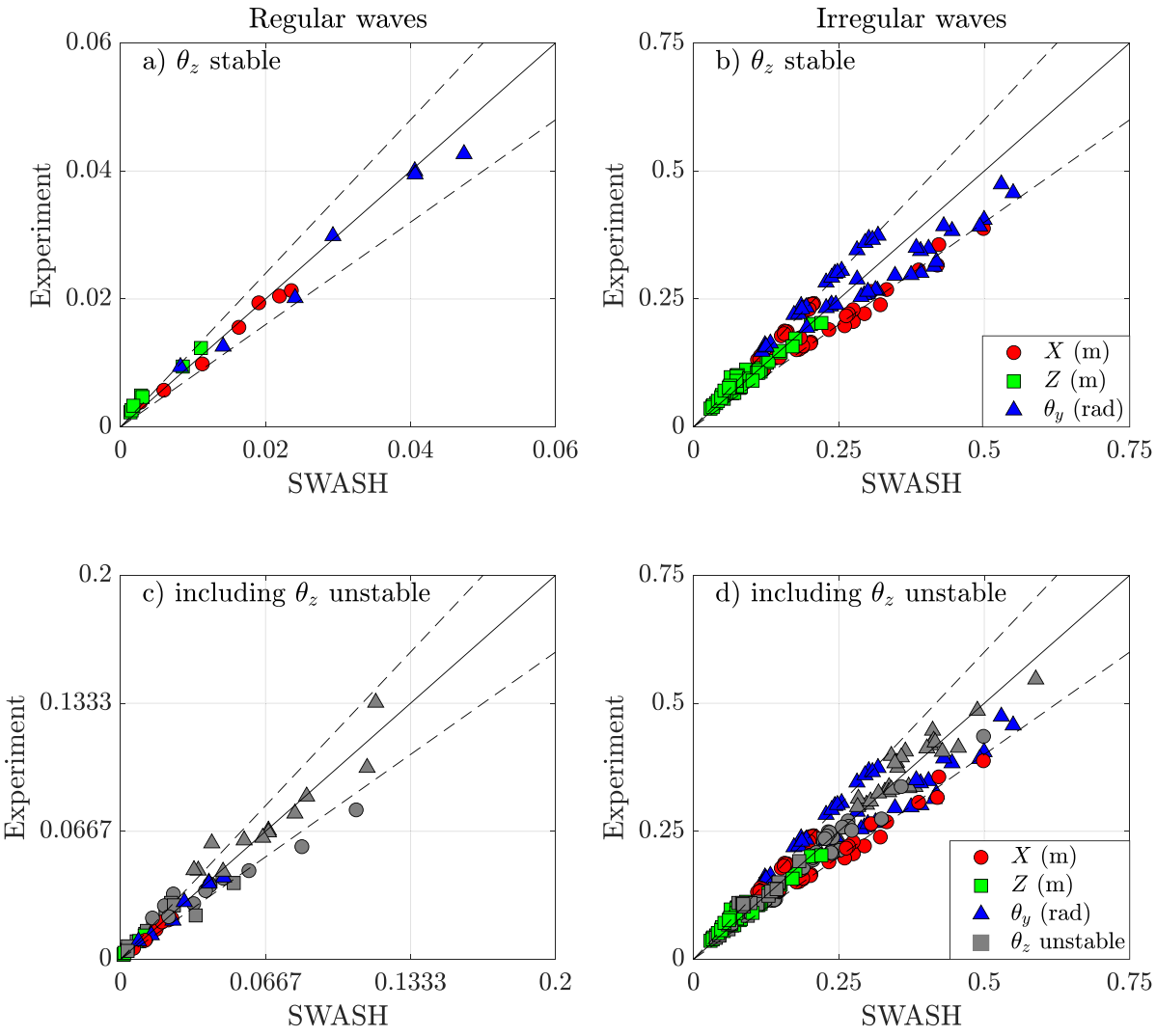

Fig. 7. Comparison of surge, heave and pitch motions from SWASH and experiment for both regular (left panels) and irregular waves (right panels) with only considering the stable conditions (top panels) and including the unstable conditions (bottom panels) highlighted in grey. For regular waves, the compared values are the response amplitudes, whereas for the irregular waves, the compared values are the significant response. The dotted lines indicate the 20% error bars.

irregular waves, especially during stable conditions (Fig. 7a, b). However, when the unstable conditions are included, for regular waves, the agreement slightly reduces. On the other hand, for irregular waves, the predictions were still comparable with the experiments (Fig. 7d). Overall, we consider the agreement reasonable as almost all SI and RB are less than 25% and almost all R and m values are larger than 0.90, see Table 3. The agreement when including the unstable conditions is better for irregular waves compared to regular waves (Table 3).

It is important to highlight here that we also observed surge-pitch and sway-roll instabilities for conditions that resulted in stable yaw response (e.g., Fig. 8). Although the displayed time window showed considerable discrepancies between the experiment and SWASH (Fig. 8c, e, g), the body motions achieved a steady-state response with a better comparison over time. Notably, the heave response for the wave condition shown in Fig. 8 compared well between SWASH and the experiment despite the mismatch observed for other body motions.

Furthermore, to compare the power absorption from SWASH and the experiment, we first computed the instantaneous power as

$$P_i = \sum_{n=1}^{3} B_{pto} \dot{l}_n^{\,2} \tag{14}$$

and the mean power ($P_{\text{mean}} = \text{mean}(P_i)$) is normalized as

$$P^n_{\text{mean}} = \frac{P_{\text{mean}}}{B_{pto}\omega^2 A^2}\,. \tag{15}$$

where A is the incident wave amplitude (for regular waves) and $A = \frac{H_s}{2}$ for irregular waves, ω is the angular wave frequency, and B_{pto} is the damping coefficient.

Fig. 9 shows the normalized power comparison between SWASH and the experiment for both regular and irregular waves. With SI < 0.05 and R > 0.9 we found good agreement between SWASH and the experiment. Although we observed noticeable discrepancies in body motions (e.g., surge and pitch) for many wave conditions (for example, Fig. 7c, g), the differences did not have a large influence on power absorption (Fig. 9). This confirms that not all modes of motion contribute equally to power absorption — the modes which are excited by instability are weakly coupled to the PTO damping (by definition), and the poorly-predicted low frequency motions in surge and pitch contribute less to power than wave frequency motions of the same amplitude. Furthermore, statistics (Table 3) provide insights on how well different variables can be predicted by WEC-SWASH in both stable and unstable conditions. The overall comparisons (Figs. 7 and 9) conclude the full validation of the WEC-SWASH and allowed us to use WEC-SWASH to benchmark the linear model.

To assess the performance of the linear model in comparison to WEC-SWASH and experimental data, we utilized the measured incident

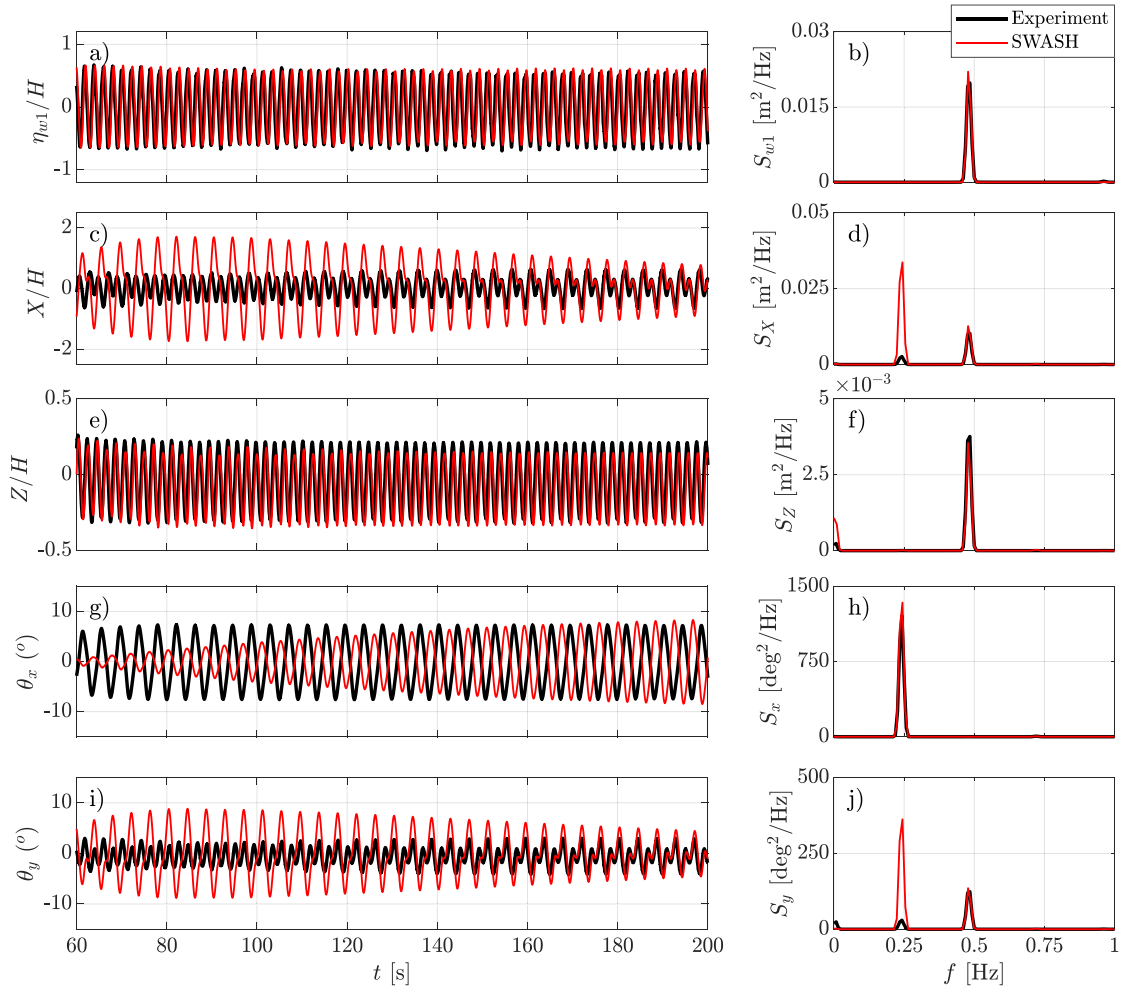

Fig. 8. Comparison of SWASH predicted and experimentally measured time series and power spectral densities (PSDs) subject to H = 0.05 m and T = 2.1 s. Panels (a) and (b) show the normalized time series and PSD of the incident wave. Panels (c), (e), (g) and (i) show the time histories of surge, heave, roll and pitch motions with their PSDs in (d), (f), (h) and (j), respectively.

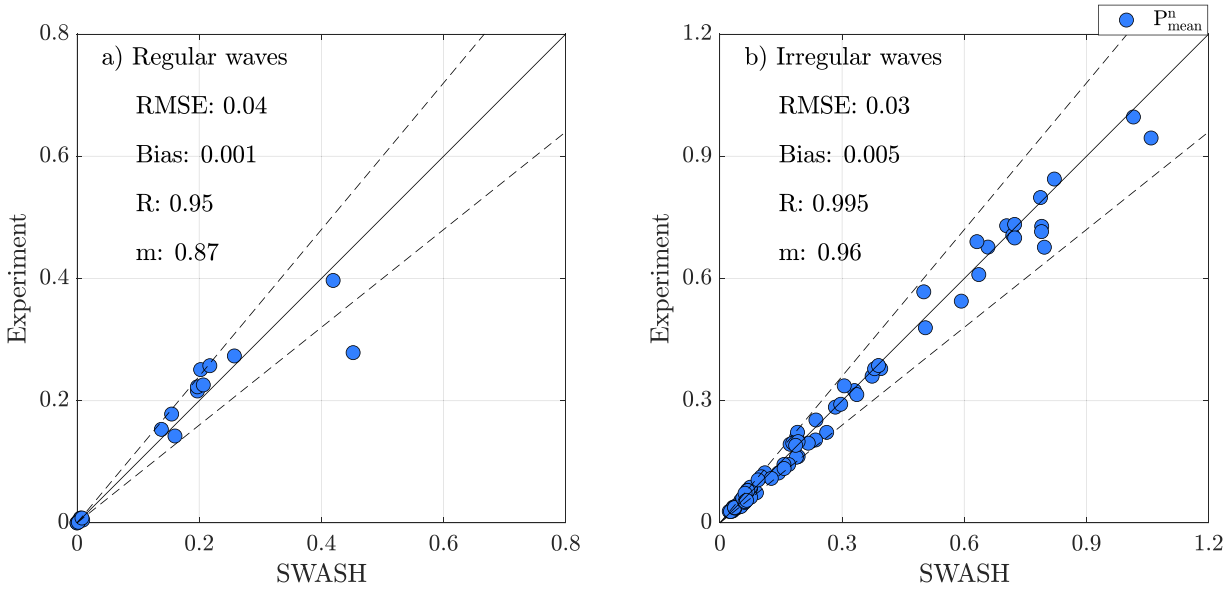

Fig. 9. Normalized mean power comparison between SWASH and experiment for both regular (a) and irregular (b) waves. The dotted lines indicate the 20% error bars.

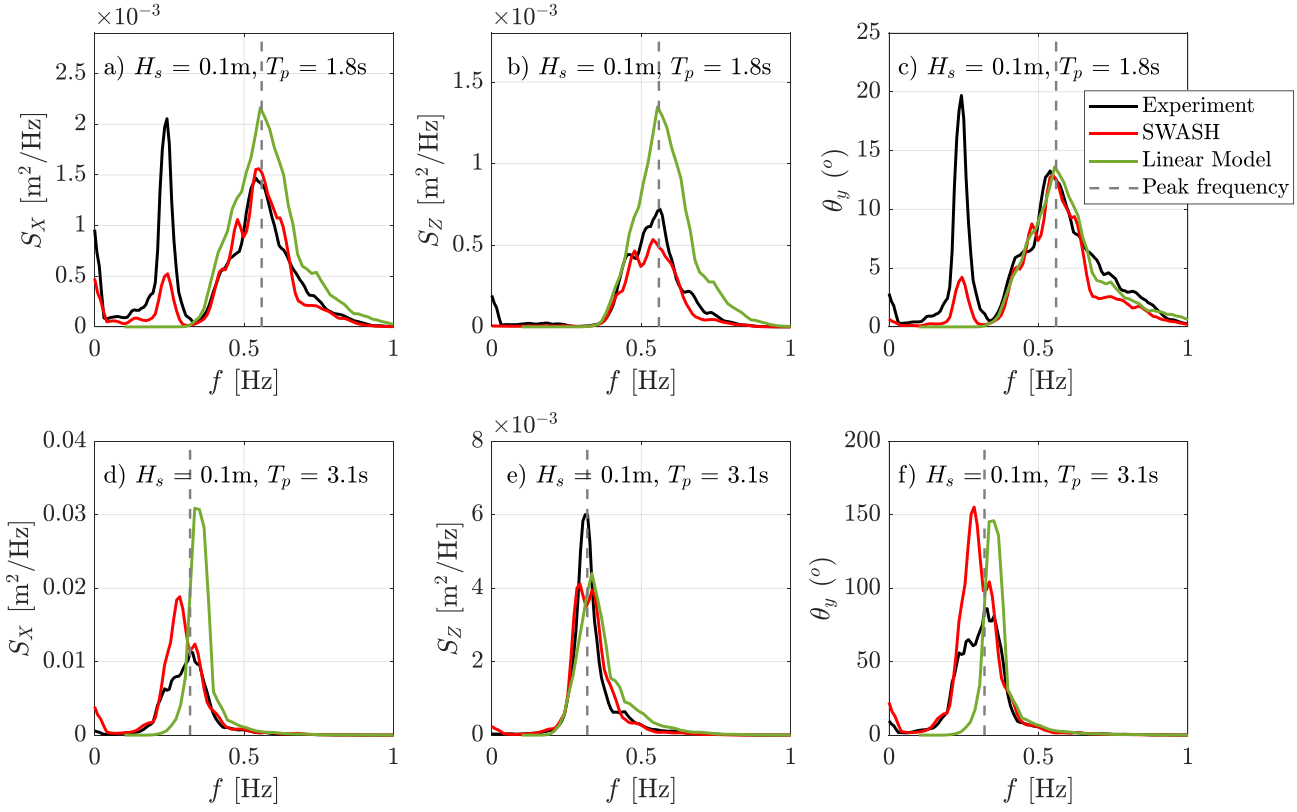

Fig. 10. Comparison of response spectra (surge, heave and pitch) from experiment, SWASH and linear model for two different wave conditions; H_s = 0.1 m, T_p = 1.8 s in top panels and H_s = 0.1 m, T_p = 3.1 s in bottom panels.

wave spectra to derive the linear response spectra. In Fig. 10, we present a comparative analysis of the response spectra, specifically for surge, heave, and pitch motions, for two distinct representative wave conditions. Notably, both wave conditions depicted in Fig. 10 resulted in stable yaw motions, as observed in the experimental and WEC-SWASH data.

Upon careful examination of Fig. 10, as well as several other cases, a consistent trend emerged. The linear model exhibited a tendency to overestimate both surge and heave motions. Existing studies have also found that linear models tend to overestimate the responses as a result of neglecting some of the hydrodynamic nonlinearities (e.g., Rafiee and Fiévez, 2015; Schubert et al., 2020; Windt et al., 2021). Furthermore, the linear model was unable to capture either the low-frequency instabilities, as observed in Fig. 10a and c, or the yaw instabilities. Additionally, we noted that the surge and pitch response peaks tended to shift towards high frequency particularly for large peak period waves, as evident in the bottom panels of Fig. 10. Overall, WEC-SWASH consistently outperforms the linear model.

4. WEC-SWASH and linear model comparison

4.1. Isolated WEC comparison

To compare and contrast the differences between the linear model and SWASH, we first compare the power absorption prediction for an isolated full-scale CETO WEC. Simulations were carried out for tether angle $\alpha_v = 60°$, submergence 3 m and water depth 34 m. This is to inform later comparison of SWASH array simulations with the results of David et al. (2022) which used this configuration. The device dimensions are otherwise as in Fig. 1 and stated in Table 1. To achieve a fair comparison between SWASH and the linear model, the same fluid density was used ($\rho = 1000$ kg/m^3) and the PTO coefficients used were the same for the two approaches: these were optimized using the linear model, to maximize the power absorption for each sea-state assuming a linear spring-damper using the MATLAB in-built global optimization toolbox. Refer to David et al. (2022) for more details on the PTO optimization procedure. The PTO coefficients were optimized based on the limits below:

$$\begin{cases} 10^6 \le K_{pto} \le 10^8 \text{ [N/m]} \\ 10^6 \le B_{pto} \le 10^8 \text{ [Ns/m]} \end{cases} \tag{16}$$

This range was fixed based on initial optimization trials and the constraint used as discussed below. Optimizing the PTO coefficients to maximize the power absorption based on linear solutions resulted in large displacement amplitudes of the WECs; therefore, we used a heave displacement constraint (HDC) in this work. In the frequency-domain modelling conducted here, we imposed this limit in a statistical sense based on the submergence depth of the WEC, which is fixed at 3 m for the full-scale comparison between SWASH and the linear model. As the device generates much of its power from the heave motion, we imposed the following heave constraint:

$$\max\left(\left|\frac{\hat{Z}}{A}\right|\right) \le \frac{3 \times 2\sqrt{2}}{\max\left(H_s\right)}, \tag{17}$$

where $\max(H_s)$ is the largest H_s of all the sea states considered in the optimization, and $|\frac{\hat{Z}}{A}|$ is the modulus of the heave response amplitude operator (RAO). This constraint is derived by assuming that the standard deviation of the heave displacement is always less than $\max\left(\left|\frac{\hat{Z}}{A}\right|\right) \cdot \frac{H_s}{4}$, since $\sigma_Z^2 = \int_0^\infty \left|\frac{\hat{Z}}{A}\right|^2 S_w(\omega)\mathrm{d}\omega$, where S_w is the power spectral density of the sea state. Taking $3/\sqrt{2}$ m as the nominal limit of the standard deviation, we arrive at Eq. (17). Note that this constraint does not guarantee that the instantaneous heave displacement will never exceed 3 m, but it is simple and sufficient for our needs. The constraint works by effectively excluding from the optimization areas in K_{pto}, B_{pto}-space where the heave constraint is violated — see the red shaded area in Fig. 12 (a).

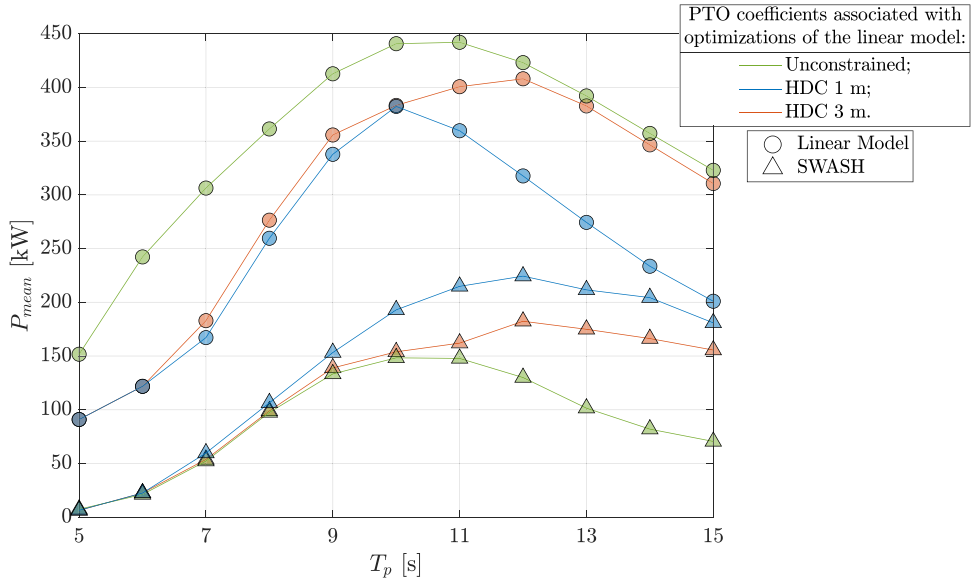

Fig. 11. Predicted mean power comparison between SWASH and linear model for different peak wave periods and significant wave height of 2 m using different sets of PTO coefficients optimized in the linear model with different displacement constraints.

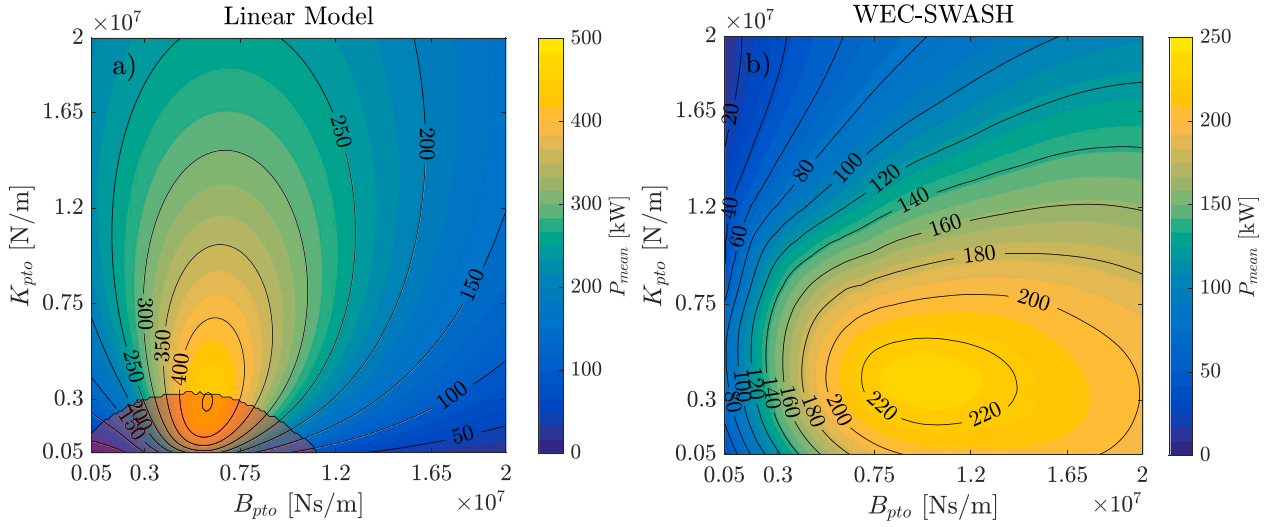

Fig. 12. Predicted mean power from the linear model (a) and WEC-SWASH (b) for different damping and stiffness coefficients subject to H_s = 2 m and T_p = 11 s. The red shades in (a) indicate the heave displacement constraint violation regimes.

When computing mean power values, the linear model figure (Fig. 11) is computed according to Eq. (7) using frequency-domain coefficients. In this paper, the values reported from SWASH are derived from a single 1.5 hr simulation corresponding to a realization of the underlying seastate with amplitudes and phases chosen randomly. This approach is expected to yield a reasonable estimate of the mean power (e.g. Saulnier et al., 2009). Fig. 11 shows the predicted mean power comparison between SWASH and the linear model for an isolated WEC with $\alpha_v = 60°$. To understand the influence of the PTO coefficients (as used to implement the heave displacement constraint), we compared the mean power absorption without the displacement constraint and with the constraints. As expected, the mean power estimation from the linear model is larger than that predicted from SWASH. However, for the linear model, the power absorption reduced upon using the PTO coefficients subject to heave constraints, whereas in SWASH the power absorption increases for these cases. This difference in power estimation implies that using SWASH instead of the linear model might give a different optimum array layout, power generation, and PTO coefficients due to two effects: (i) at a given frequency (and amplitude) SWASH gives a different result than the linear model; (ii) the differences between SWASH and the linear model are a function of frequency (and amplitude) so that if the optimization was carried out using SWASH, different parts of the wave frequency spectrum would be emphasized or targeted by the optimization procedure which could lead to a different result. Of course, the optimizations should ultimately be performed with a wave-to-wire model incorporating additional system dynamics (see e.g., Penalba and Ringwood, 2020 for considerations concerning choice of model complexity). Note, for the constrained cases, the optimization determining the PTO coefficients satisfying the constraint were computed with $\max(H_s)$ fixed as 4 m. As might be expected, the damping coefficients increased drastically (14%–450%) for different wave heights and wave periods with the constrained case (HDC = 3 m), whereas the stiffness coefficient varied moderately (0.05%–18%) compared to the unconstrained case.

PTOs play a crucial role in power generation, force constraints, and most importantly, the economic performance of WECs. Most early-stage studies use linear PTO or linearized representations of nonlinear PTO (Rafiee and Fiévez, 2015; Rijnsdorp et al., 2018; Schubert et al.,

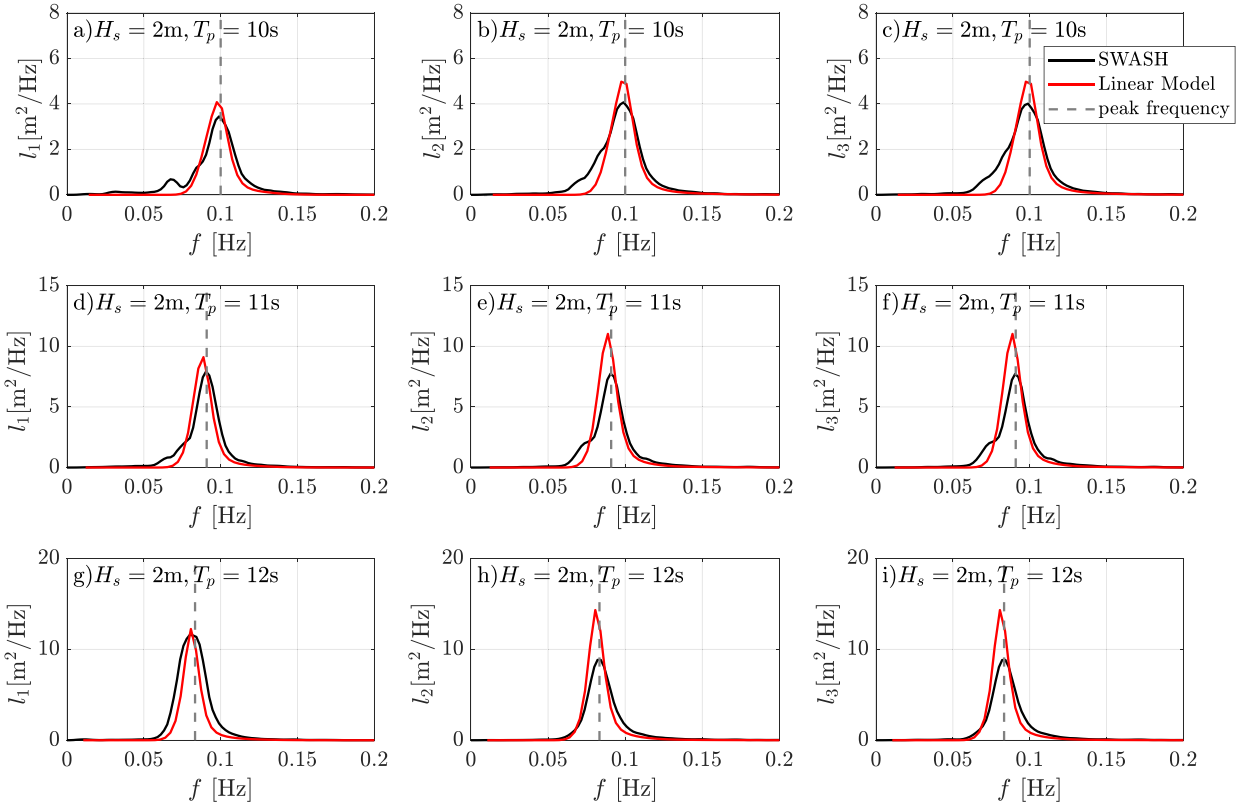

Fig. 13. Comparison of tether extension for an isolated WEC with $\alpha_v = 60°$ and exposed to a significant wave height of 2 m and peak wave periods of 10 s (a-c), 11 s (d-e), and 12 s (g-i).

2020; Sergiienko et al., 2018). For maximizing power generation, the PTO coefficients (stiffness and damping) are tuned such that the power-generating modes (for multi-mode WECs) are in resonance. Due to its computational expense, it is practically impossible to optimize the PTO coefficients using SWASH, so we have used the coefficients optimized using the linear model in SWASH. However, whether the linear model-optimized coefficients are the optimal coefficients for SWASH is not clear — the results in Fig. 11 suggest that they are not. To address this, we carried out additional simulations (for an isolated WEC) using both the linear model and SWASH. For this purpose, we chose a site-specific dominant wave condition $H_s = 2$ m, $T_p = 11$ s based on measurements recorded at Torbay near Albany, Western Australia, which has been proposed as a wave energy development site (Cuttler et al., 2020).

For this test case, the PTO coefficients range was fixed as shown in Fig. 12. As the linear model is computationally efficient, we considered discrete fine intervals of coefficients (200 × 200) and linearly interpolated them to obtain the spatial distribution. For illustrative purposes, the region of HDC violation is highlighted in red shades (Fig. 12a). For SWASH, due to its computational expense, it is not feasible to compute a similar number of simulations. Therefore, we strategically picked the combination of coefficients and limited the number of simulations to about 65. Using a locally weighted polynomial regression fit (a 'lowess' fit), we obtained the surface variations for SWASH. With a coefficient of determination (R^2) of 0.99 and Root Mean Square Error (RMSE) = 2 kW, we expect the power variation for different PTO combinations to be close to accurate.

Unlike the linear model, we observed a relatively broad power absorption peak from SWASH (Fig. 12). As might be expected, the optimum coefficients for the maximum power absorption were found to be different in the two models. The stiffness and damping coefficients of the maximum power were slightly larger in SWASH than in the linear model. This confirms that the optimum coefficients from the linear model may not be the optimum coefficients for SWASH. This suggests that the optimum PTO coefficients for arrays, if optimized while accounting for nonlinear WEC interactions, would be different from those optimized using a linear model. Furthermore, if the mean power absorption is of primary interest, the difference in power absorption (from SWASH) using the linear model-optimized and SWASH-optimized coefficients was about 30%, emphasizing the importance of accounting for nonlinearity.

To further understand the differences between the two models, we focused on the tether extensions for three representative wave conditions: $H_s = 2$ m, and T_p varied between 10, 11, and 12 s, respectively. The adopted wave conditions were based on the maximum power absorption conditions from both models (Fig. 11) and the predominant wave condition at Torbay, Western Australia.

Fig. 13 shows the tether extension spectra comparison between SWASH and the linear model with a maximum HDC of 3 m for the three representative wave conditions, with identical PTO coefficients. Notably, all three conditions resulted in mild yaw instability ($2.5° > \sigma_z > 1°$) in WEC-SWASH. As a result of yaw instability, we observed some nonlinearities in the tether extension spectra (e.g., Fig. 13a) from WEC-SWASH, whereas such nonlinearities and yaw instabilities were impossible to predict using the linear model. Furthermore, due to the coupled surge-pitch resonance, the prediction from WEC-SWASH for tether extension l_1 reveals a secondary peak (Fig. 13a) that is driven parametrically. The linear model does not predict this secondary peak (where surge and pitch are also coupled). The overall comparison (Fig. 13) shows that the linear model generally overpredicted the tether extensions and thereby the power absorption (e.g., Fig. 11). However, it is to be noted that in Fig. 12 we observed a (suboptimal) region where the power absorption in SWASH is larger than in the linear model, notably for higher damping and lower stiffness coefficients.

4.2. Wave farm comparison

Having validated SWASH and studied the behaviour of a single WEC, we now extend the comparison to arrays. In WEC-SWASH, the

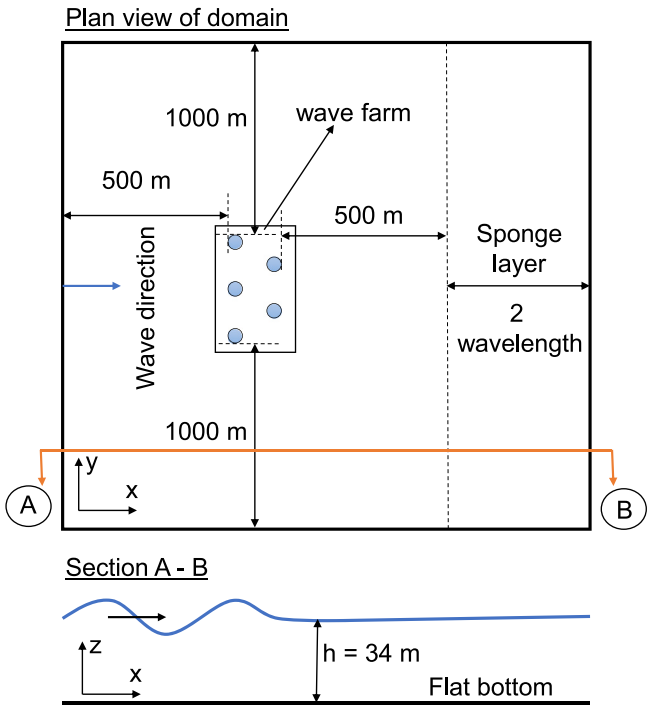

Fig. 14. Plan and sectional view of the SWASH model domain used to compare with the linear frequency domain model.

wave boundary was fixed at 500 m (offshore) from the wave farm (Fig. 14). Similar to Rijnsdorp et al. (2020), cyclic boundary conditions were used along the lateral boundaries, and to minimize the effect of lateral boundary conditions, a distance of 1 km was fixed from the edge of the wave farm to the lateral boundaries. Furthermore, to avoid wave reflections, a sponge layer 2 × the peak wavelength was adopted at the wave absorber end. For the model comparisons, we considered two wave farms composed of 5 WECs arranged in one and two rows, referred to as array-A and array-B, respectively (see Fig. 15a and d). These layouts and associated PTO coefficients were based on the converged solutions from the multi-objective optimization carried out by the authors for site-specific wave conditions using HDC 3 m. For more details, readers are referred to David et al. (2022).

Fig. 15 shows the predicted mean power comparison between WEC-SWASH and the linear model for the wave farms composed of 5-WECs subjected to irregular waves of T_p = 11 s and H_s from 0.5 to 3 m, associated with an underlying JONSWAP spectrum in each case (γ = 3.3). For H_s < 1 m, the models' predictions of mean array power are comparable, with the linear model predicting approximately 5% higher than SWASH (Fig. 15b, e). With an increase in wave height, the difference increased to about 45% for H_s = 2 m.

As is well known, a quadratic growth in power absorption was observed from the linear model, whereas WEC-SWASH predicts an approximately linear growth in this range. This is consistent for both arrays. To understand the array interactions and the variation in power absorption of individual WECs in relation to the array power, we computed the ratio of individual WEC power to the array power in Fig. 15c, f. The ratio from the linear model does not change with wave height, whereas for SWASH we observed significant fluctuations in the ratio for different wave heights. Notably, for array-B, the linear model predicted that the WECs in the second row (i.e., WECs 4 and 5) generated more power than WECs in the first row (Fig. 15f). The opposite trend was predicted for SWASH.

On comparing the q-factor for the two chosen wave farms (Fig. 16) using two different models, we observed a decreasing trend with increasing wave heights for WEC-SWASH (note that this q-factor is computed using results from an individual WEC in SWASH). The q-factor is defined as the ratio of the power of the array to the power absorbed from an isolated WEC times the number of WECs in the array (e.g., Babarit, 2013). Notably, the difference in the q-factor between the two models is smaller for array-B, whereas the difference increases with increasing wave height for array-A. Interestingly, the WEC-SWASH predicted q-factor exceeded the linear model predicted value for array-B (for H_s < 2 m). This implies that array interaction can be complex and it requires a relevant nonlinear model to fully understand these interactions.

It is important to highlight here that the same PTO coefficients were used in SWASH and the linear model, and that the coefficients were optimized for power absorption using the linear model. Furthermore, the PTO coefficients were those optimized for a site-specific wave climate (readers are referred to David et al. (2022). We did not attempt to optimize the array PTO coefficients for WEC-SWASH, given the computational expense. For example, the 5-WEC cases took about 8 h on ≈ 100 cores (CPUs) for a single wave condition (of 40 mins duration), whereas the linear model took less than a minute on a four-core desktop PC. However, if the PTO coefficients were optimized for WEC-SWASH, it would influence the array interactions and the resulting power absorption could be different.

The tether extension spectra for the two wave farms (Fig. 15a, d) subjected to H_s = 2 m and T_p = 11 s are compared in Fig. 17. We observed that the WECs exhibit symmetrical responses in terms of the spectral shape and the magnitude for both wave farms and from both approaches. Similar to the power absorption (Fig. 15), the linear model predictions for the tether extensions were slightly larger than WEC-SWASH. The linear model predictions also revealed a secondary peak that could be related to array interactions or the coupled surge-pitch resonance. Such peaks were not observed from WEC-SWASH. We also found that power absorption and tether extensions are highly sensitive to the PTOs settings (Figs. 15, 17).

In an attempt to gain better insights into the interactions within these two arrays, we conducted a comparative analysis of the wave surface elevation spectra extracted from multiple points in the SWASH domain situated between the WECs in the arrays. This analysis was performed across different wave heights, as depicted in Fig. 18. For illustrative purposes, the spectra were normalized with respect to the maximum of the incident wave spectra.

For array A, for which the linear q-factor is rather high and interactions therefore important, the q-factor and fraction of power absorbed by each WEC changes significantly with amplitude. This is reflected in the free surface elevations, with little relative change at P2 in the inner gap in the array between 1–2 m H_s, but a large change at P1 in the outer gap. Conversely for array B, for which the linear q-factor is close to 1, neither the q-factor nor the fraction of power absorbed by each WEC changes significantly with amplitude. This is reflected in the relatively uniform change in wave heights between 1 m and 2 m at the points chosen — the array is becoming less efficient with amplitude, but only at the rate an individual device does. These results tend to support the understanding referred to in the Introduction that minimizing destructive interference is a more practical objective than maximizing constructive interference. At the very least, the results show that for these arrays, it is challenging to maintain constructive interference at different amplitudes with the same PTO settings.

5. Discussion and conclusion

This study addresses the differences in power absorption estimates for WEC arrays obtained using a linear frequency-domain model and WEC-SWASH which accounts for some nonlinear hydrodynamic effects. The WEC-SWASH model was first validated against experimental data for the measured body responses and power absorption (for an isolated WEC). Validation revealed that WEC-SWASH was able to reproduce the measured body responses with less than 25% error (for irregular waves). Furthermore, the WEC-SWASH estimated hydrodynamic power

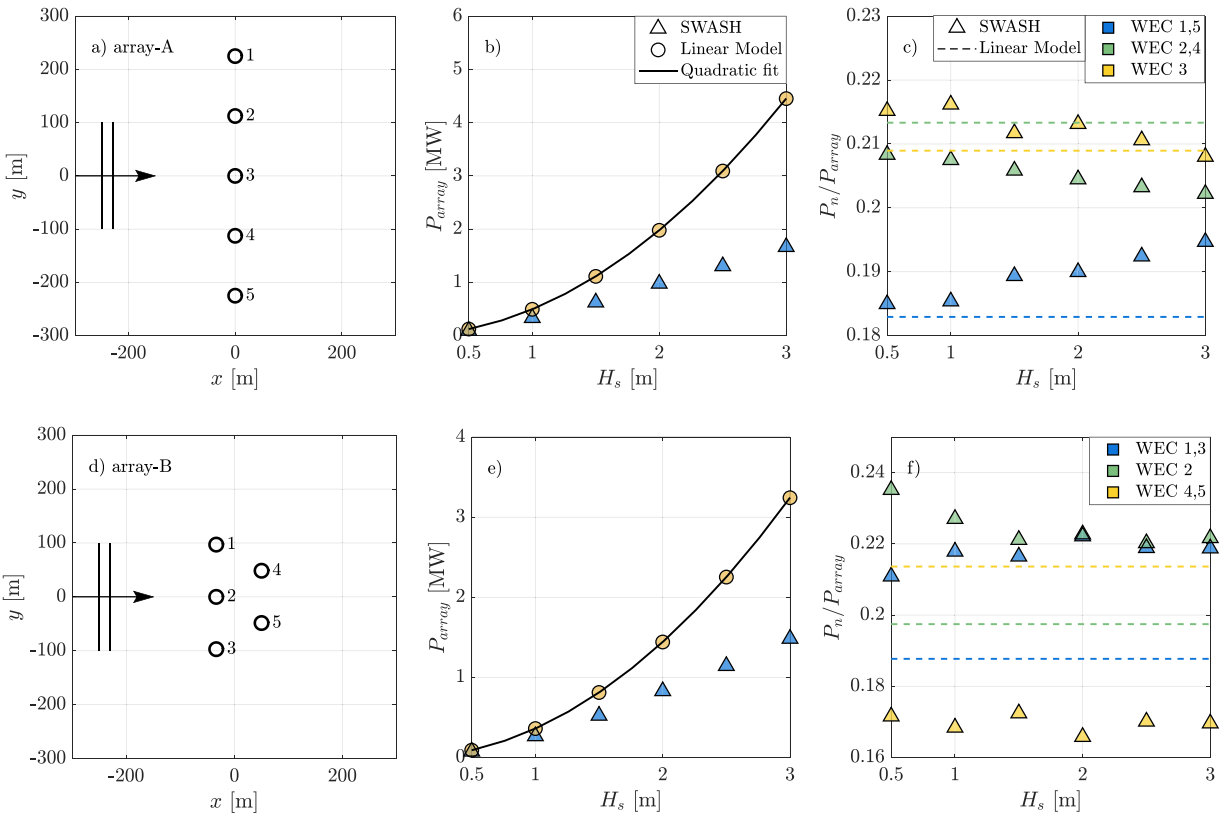

Fig. 15. Predicted mean power comparison between SWASH and linear model for the wave farms composed of 5-WECs arranged in a single row (a), and two rows (d) exposed to various significant wave heights from 0.5 m to 3 m with a peak wave period of 11 s. (b) and (e) the mean array power. (c), (f) the mean power from individual WECs in the array (symmetry holds in SWASH to within 1% in mean power).

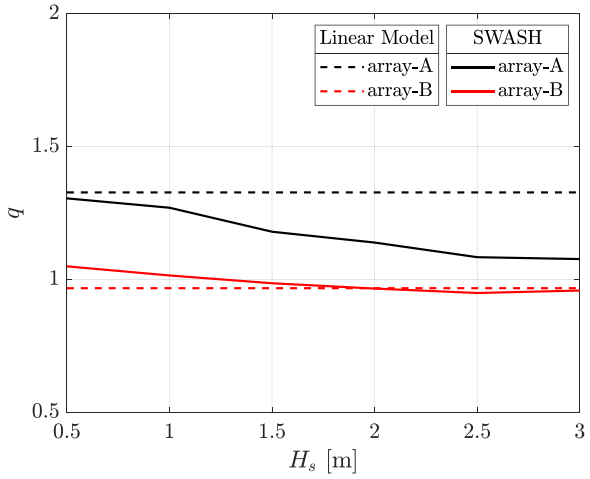

Fig. 16. q factor comparison as a function of H_s for the two wave farms using SWASH and the linear model (T_p = 11 s).

absorption was found to be in good agreement (less than 5% error) with the experiments. This validates the model predictions and provides confidence in benchmarking WEC-SWASH to compare with the linear model.

The usefulness in practice of array optimization with a linear model is still unclear, and this may be addressed (for this type of WEC) with a validated WEC-SWASH model which does a good job of reproducing basin test results. The results in this study show that at a given frequency, WEC-SWASH gives less power than the linear model, but that the shape of the power curve in amplitude and frequency space is different for WEC-SWASH and the linear model. This suggests that the true hydrodynamically optimal array is not the same as the linearly optimal array. It is tempting to consider a scheme where WEC-SWASH is used to tune amplitude-dependent coefficients for a single WEC which then interact linearly for multiple WECs in the optimization. However, Fig. 15 shows that the array interactions themselves are nonlinear, making this approach liable to inaccuracy as well. It is striking that the way an array 'behaves' may be different in the two models - e.g., whether the front or back row absorbs more power in Fig. 15. In this case the array with higher q-factor was more sensitive to nonlinearity. Previous work (David et al., 2022) shows that when multiple objectives are considered, higher-q and lower-q solutions can perform similarly in terms of overall metrics; to avoid sensitivity to hydrodynamic nonlinearity it may be preferable to avoid higher-q solutions. This suggestion requires additional investigation.

It is important to highlight some of the limitations associated with the numerical models used in this work. WEC-SWASH was able to incorporate nonlinearity in the incident waves, but the numerical method restricts the body motions to be relatively small compared to the flow grid (Rijnsdorp et al., 2018). Furthermore, due to the shallow submergence of the WEC, we observed periodic drying and flooding on top of the device, and as a result, we were unable to run large wave conditions (H_s > 3 m). Neither model incorporates viscous drag effects, although we do not expect these to be the dominant hydrodynamic nonlinearity for this WEC (e.g., McCauley et al., 2023). The linear frequency-domain model uses hydrodynamic coefficients obtained assuming linear potential flow theory.

WEC-SWASH simulations are computationally expensive relative to the linear solution; however, they are still an order of magnitude less expensive than CFD simulations (Rijnsdorp et al., 2018). Therefore, it may be possible to carry out a limited number of simulations from WEC-SWASH to obtain trends in power absorption as a function of

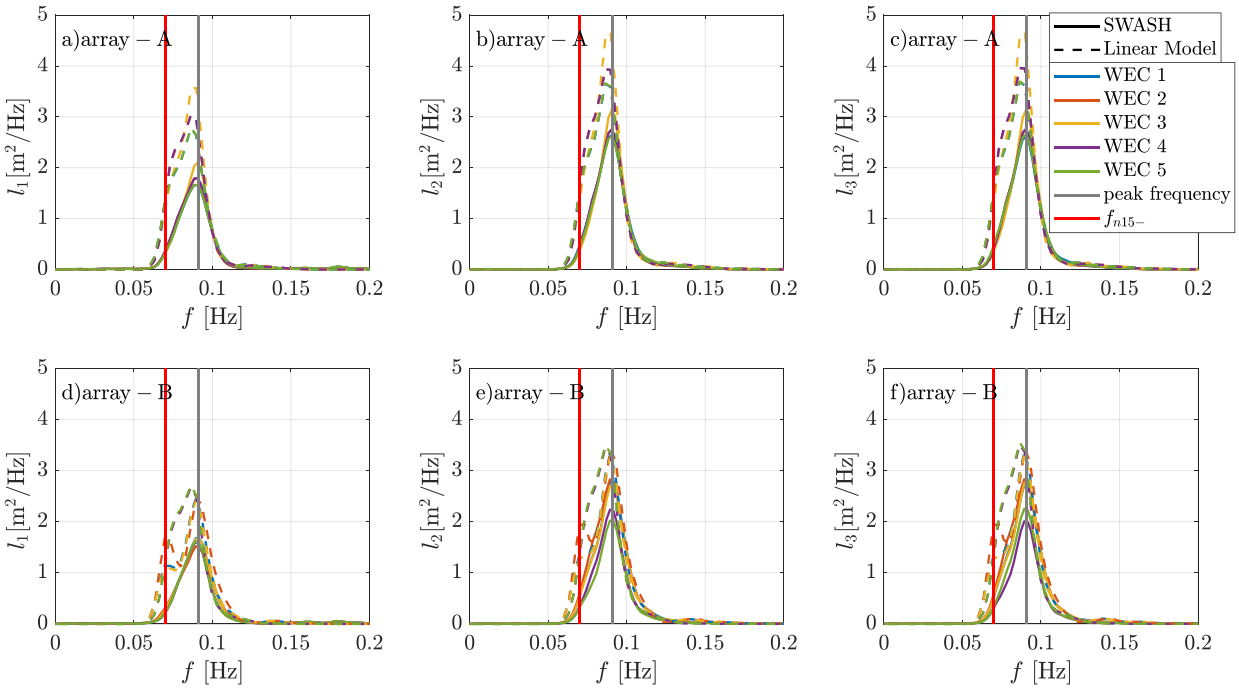

Fig. 17. Comparison of tether extensions for individual WECs in the array-A (a,b,c) and array-B (d,e,f) exposed to a significant wave height of 2 m with a peak wave period of 11 s with $\alpha_v = 60°$.

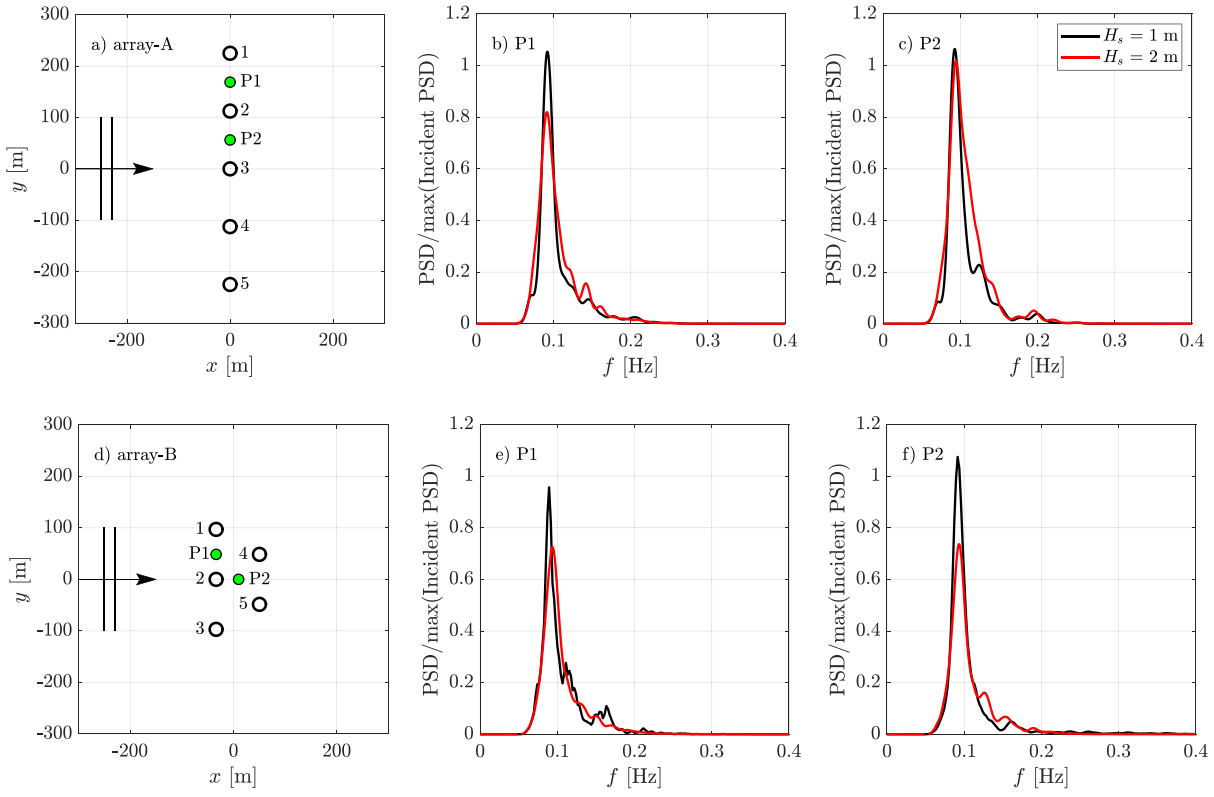

Fig. 18. Comparison of normalized surface elevation spectra from WEC-SWASH at two different locations for the two representative arrays (H_s = 1 m, 2 m, T_p = 11 s).

wave steepness or PTO coefficients that could then be used to fit or apply a correction factor to the linear model predictions. If the nonlinearities in the body response can be quantified, it may be possible to even parameterize these effects internally in the linear model. Results also indicated that not all the modes of motion contribute to power absorption equally. Furthermore, WEC-SWASH was able to capture some of the motion instabilities, in particular yaw instabilities observed during the experiments. However, the predicted yaw magnitude from SWASH was about 4 to 46% larger than that measured experimentally. This could be due to lack of viscous force in the model and thereby damping on the yaw motion. The aforementioned possibilities are not investigated in this present work and are considered for future works.

Table 3
Statistical measures (Scatter Index — SI, Relative Bias — RB, correlation coefficient — R and slope — m) computed using simulated and measured amplitudes of the surge, X, heave, Z and pitch, θ_y for regular and irregular wave conditions that resulted in stable yaw (θ_z) motions and, in brackets, including both the conditions that resulted in unstable θ_z motions and the yaw stable conditions.

	Regular waves			Irregular waves		
	X	Z	θ_y	X	Z	θ_y
SI	0.09 (0.34)	0.25 (0.31)	0.09 (0.14)	0.23 (0.18)	0.13 (0.12)	0.19 (0.14)
RB	0.05 (0.12)	−0.24 (−0.07)	0.05 (−0.03)	0.08 (0.07)	−0.05 (−0.05)	0.02 (0.01)
R	0.99 (0.97)	0.99 (0.94)	0.99 (0.97)	0.94 (0.94)	0.97 (0.97)	0.89 (0.90)
m	0.90 (0.67)	0.97 (0.79)	0.93 (0.98)	0.66 (0.63)	0.86 (0.91)	0.63 (0.95)

CRediT authorship contribution statement

Daniel Raj David: Writing – original draft, Validation, Methodology, Formal analysis, Data curation, Conceptualization. **Hugh Wolgamot:** Writing – review & editing, Supervision, Methodology, Conceptualization. **Adi Kurniawan:** Writing – review & editing, Supervision, Methodology, Conceptualization. **Jeff Hansen:** Writing – review & editing, Supervision, Methodology, Funding acquisition, Conceptualization. **Dirk Rijnsdorp:** Writing – review & editing, Supervision, Software, Methodology.

Declaration of competing interest

The authors declare that they have no known competing financial interests or personal relationships that could have appeared to influence the work reported in this paper.

Data availability

All data, models and codes that support the findings of this study are available from the corresponding author upon request.

Acknowledgements

This project forms part of a Ph.D. study by DRD at the University of Western Australia which is supported by the Commonwealth Government, Australia through an Australian Government Research Training Program Scholarship. Funding was provided by the Australian Renewable Energy Agency, Research and Development Programme (grant number 2015RND086 in partnership with Carnegie Clean Energy) and the Wave Energy Research Centre, Australia (through funding provided by the Western Australian Government, via the Department of Primary Industries and Regional Development (DPIRD), and the University of Western Australia). Supercomputer access was provided by the Pawsey Supercomputing Centre with funding from the Australian Government and the Government of Western Australia. HW was supported by an Australian Research Council (ARC) Early Career Fellowship (DE200101478). We thank Guy McCauley, Jana Orszaghova, Thobani Hlophe, Mario Conde, William Edge for fruitful discussions that benefited the work. Finally, we appreciate the suggestions of two anonymous reviewers.

References

Agamloh, E.B., Wallace, A.K., von Jouanne, A., 2008. Application of fluid-structure interaction simulation of an ocean wave energy extraction device. Renew. Energy 33 (4), 748–757.
Babarit, A., 2013. On the park effect in arrays of oscillating wave energy converters. Renew. Energy 58, 68–78.
Budal, K., 1977. Theory for absorption of wave power by a system of interacting bodies. J. Ship Res. 21 (4), 248–253.
Cuttler, M.V., Hansen, J.E., Lowe, R.J., 2020. Seasonal and interannual variability of the wave climate at a wave energy hotspot off the southwestern coast of Australia. Renew. Energy 146, 2337–2350.
David, D.R., Kurniawan, A., Wolgamot, H., Hansen, J.E., Rijnsdorp, D., Lowe, R., 2022. Nearshore submerged wave farm optimisation: A multi-objective approach. Appl. Ocean Res. 124, 103225.
Davidson, J., Costello, R., 2020. Efficient nonlinear hydrodynamic models for wave energy converter design—A scoping study. J. Mar. Sci. Eng. 8 (1), 1–65.
Davidson, J., Kalmár-Nagy, T., Habib, G., 2022. Parametric excitation suppression in a floating cylinder via dynamic vibration absorbers: a comparative analysis. Nonlinear Dynam. 110 (2), 1081–1108.
Faedo, N., Olaya, S., Ringwood, J.V., 2017. Optimal control, MPC and MPC-like algorithms for wave energy systems: An overview. IFAC J. Syst. Control 1, 37–56.
Faedo, N., Peña-Sanchez, Y., Pasta, E., Papini, G., Mosquera, F.D., Ferri, F., 2023. SWELL: An open-access experimental dataset for arrays of wave energy conversion systems. Renew. Energy 212, 699–716.
Faedo, N., Scarciotti, G., Astolfi, A., Ringwood, J.V., 2019. Moment-based constrained optimal control of an array of wave energy converters. In: Proceedings of the American Control Conference 2019-July. American Automatic Control Council, pp. 4797–4802.
Falnes, J., 2002. Ocean Waves and Oscillating Systems: Linear Interaction Including Wave Energy Extraction. Cambridge Univ. Press, p. 220.
Falnes, J., Budal, K., 1982. Wave-power absorption by parallel rows of interacting oscillating bodies. Appl. Ocean Res. 4 (4), 194–207.
Folley, M., 2016. Numerical Modelling of Wave Energy Converters. Elsevier Ltd.
Fusco, F., Gilloteaux, J.C., Ringwood, J., 2010. A study on prediction requirements in time-domain control of wave energy converters. IFAC Proc. Vol. (IFAC-PapersOnline) 43 (20), 372–377.
Giorgi, G., Davidson, J., Habib, G., Bracco, G., Mattiazzo, G., Kalmár-Nagy, T., 2020. Nonlinear dynamic and kinematic model of a spar-buoy: Parametric resonance and yaw numerical instability. J. Mar. Sci. Eng. 8 (7).
Giorgi, G., Ringwood, J.V., 2017. Computationally efficient nonlinear Froude–Krylov force calculations for heaving axisymmetric wave energy point absorbers. J. Ocean Eng. Mar. Energy 3 (1), 21–33.
Giorgi, G., Ringwood, J.V., 2019. A compact 6-DoF nonlinear wave energy device model for power assessment and control investigations. IEEE Trans. Sustain. Energy 10 (1), 119–126.
Göteman, M., Giassi, M., Engström, J., Isberg, J., 2020. Advances and challenges in wave energy park optimization—A review. Front. Energy Res. 8:26.
Hals, J., Falnes, J., Moan, T., 2010. Constrained optimal control of a heaving buoy wave-energy converter. J. Offshore Mech. Arct. Eng. 133, 1–15.
Karthikeyan, A., Previsic, M., Scruggs, J., Chertok, A., 2019. Non-linear model predictive control of wave energy converters with realistic power take-off configurations and loss model. In: CCTA 2019 - 3rd IEEE Conference on Control Technology and Applications. IEEE, pp. 270–277.
Kurniawan, A., Grassow, M., Ferri, F., 2019. Numerical modelling and wave tank testing of a self-reacting two-body wave energy device. Ships Offshore Struct. 14 (sup1), 344–356.
Lam, D., Simpson, R., 1976. Centered differencing and the box scheme for diffusion convection problems. J. Comput. Phys. 22 (4), 486–500.
Li, Y., Yu, Y.H., 2012. A synthesis of numerical methods for modeling wave energy converter-point absorbers. Renew. Sustain. Energy Rev. 16 (6), 4352–4364.
McCauley, G., Wolgamot, H., Draper, S., Orszaghova, J., 2023. Hybrid axisymmetric model for forced heave of a shallowly submerged cylindrical wave energy converter. Flow 3, E36.
McCauley, G., Wolgamot, H., Orszaghova, J., Draper, S., 2018. Linear hydrodynamic modelling of arrays of submerged oscillating cylinders. Appl. Ocean Res. 81, 1–14.
McIver, P., 1994. Some hydrodynamic aspects of arrays of wave-energy devices. Appl. Ocean Res. 16 (2), 61–69.
Orszaghova, J., Wolgamot, H., Draper, S., Taylor, P.H., Rafiee, A., 2020. Onset and limiting amplitude of yaw instability of a submerged three-tethered buoy. Proc. R. Soc. A: Math., Phys. Eng. Sci. 476 (2235), 20190762.
Orszaghova, J., Wolgamot, H., Draper, S., Taylor, R.E., Taylor, P.H., Rafiee, A., 2019. Transverse motion instability of a submerged moored buoy. Proc. R. Soc. A: Math., Phys. Eng. Sci. 475 (2221), 20180459.
O'Sullivan, A.C., Lightbody, G., 2017. Co-design of a wave energy converter using constrained predictive control. Renew. Energy 102, 142–156.
Özkan-Haller, H.T., Haller, M.C., Cameron McNatt, J., Porter, A., Lenee-Bluhm, P., 2017. Analyses of wave scattering and absorption produced by WEC arrays: Physical/numerical experiments and model assessment. In: Marine Renewable Energy: Resource Characterization and Physical Effects. Springer International Publishing, pp. 71–97.

Peckolt, J., Lucas, J., Jan, P., Friedhoff, B., 2015. Cable robots for experimental investigations of wave energy converters. In: Proceedings of the 11th European Wave and Tidal Energy Conference. Nantes, France, pp. 1–7, 6–11 September.

Penalba, M., Giorgi, G., Ringwood, J.V., 2017a. Mathematical modelling of wave energy converters: A review of nonlinear approaches. Renew. Sustain. Energy Rev. 78, 1188–1207.

Penalba, M., Mérigaud, A., Gilloteaux, J.C., Ringwood, J.V., 2017b. Influence of nonlinear Froude–Krylov forces on the performance of two wave energy points absorbers. J. Ocean Eng. Mar. Energy 3 (3), 209–220.

Penalba, M., Ringwood, J.V., 2020. Systematic complexity reduction of wave-to-wire models for wave energy system design. Ocean Eng. 217, 107651.

Penalba, M., Touzón, I., Lopez-Mendia, J., Nava, V., 2017c. A numerical study on the hydrodynamic impact of device slenderness and array size in wave energy farms in realistic wave climates. Ocean Eng. 142 (August 2016), 224–232.

Rafiee, A., Fiévez, J., 2015. Numerical prediction of extreme loads on the CETO wave energy converter. In: 11th European Wave and Tidal Energy Conference. Nantes, France.

Rijnsdorp, D.P., Hansen, J.E., Lowe, R.J., 2018. Simulating the wave-induced response of a submerged wave-energy converter using a non-hydrostatic wave-flow model. Coast. Eng. 140, 189–204.

Rijnsdorp, D.P., Hansen, J.E., Lowe, R.J., 2020. Understanding coastal impacts by nearshore wave farms using a phase-resolving wave model. Renew. Energy 150, 637–648.

Ringwood, J.V., Bacelli, G., Fusco, F., 2014. Energy-maximizing control of wave-energy converters: The development of control system technology to optimize their operation. IEEE Control Syst. Mag. 34 (5), 30–55.

Saulnier, J.-B., Ricci, P., Clément, A.H., Falcão, A., 2009. Mean power output estimation of WECs in simulated sea-states. In: Proceedings of the 8th European Wave and Tidal Energy Conference. Uppsala, Sweden (September), pp. 891–900.

Schubert, B.W., Robertson, W.S., Cazzolato, B.S., Ghayesh, M.H., 2020. Linear and nonlinear hydrodynamic models for dynamics of a submerged point absorber wave energy converter. Ocean Eng. 197, 106828.

Scruggs, J.T., Lao, Y., 2019. A new passivity-based nonlinear causal control technique for wave energy converters with finite stroke. In: Proceedings of the American Control Conference. pp. 5472–5479.

Sergiienko, N.Y., Rafiee, A., Cazzolato, B.S., Ding, B., Arjomandi, M., 2018. Feasibility study of the three-tether axisymmetric wave energy converter. Ocean Eng. 150, 221–233.

Stavropoulou, C., Goude, A., Katsidoniotaki, E., Göteman, M., 2023. Fast time-domain model for the preliminary design of a wave power farm. Renew. Energy 219, 119482.

Stelling, G., Zijlema, M., 2003. An accurate and efficient finite-difference algorithm for non-hydrostatic free-surface flow with application to wave propagation. Internat. J. Numer. Methods Fluids 43 (1), 1–23.

Stratigaki, V., Troch, P., Stallard, T., Forehand, D., Kofoed, J.P., Folley, M., Benoit, M., Babarit, A., Kirkegaard, J., 2014. Wave basin experiments with large wave energy converter arrays to study interactions between the converters and effects on other users in the sea and the coastal area. Energies 7 (2), 701–734.

Tarrant, K., Meskell, C., 2016. Investigation on parametrically excited motions of point absorbers in regular waves. Ocean Eng. 111, 67–81.

Thomas, G.P., Evans, D.V., 1981. Arrays of three-dimensional wave-energy absorbers. J. Fluid Mech. 108, 67–88.

Venugopal, V., Smith, G.H., 2007. Wave climate investigation for an array of wave power devices. In: Proceedings of the 7th European Wave and Tidal Energy Conference. Porto, Portugal, pp. 11–14.

Welch, P.D., 1967. The use of Fast Fourier Transform for the estimation of power spectra: A method based on time averaging over short, modified periodograms. IEEE Trans. Audio Electroacoust. 15, 70–73.

Westphalen, J., 2011. Extreme Wave Loading on Offshore Wave Energy Devices using CFD (Ph.D. thesis). Faculty of Science and Technology, University of Plymouth.

Windt, C., Faedo, N., Penalba, M., Dias, F., Ringwood, J.V., 2021. Reactive control of wave energy devices – the modelling paradox. Appl. Ocean Res. 109 (February).

Wolgamot, H.A., Fitzgerald, C.J., 2015. Nonlinear hydrodynamic and real fluid effects on wave energy converters. Proc. Inst. Mech. Eng., A: J. Power Energy 229 (7), 772–794.

Zhang, Y., Teng, B., Gou, Y., 2021. Nonlinear modelling of a point-absorber wave energy converter based on the weak-scatterer approximation. Ocean Eng. 239 (August), 109924.

Zijlema, M., Stelling, G., Smit, P., 2011. SWASH: An operational public domain code for simulating wave fields and rapidly varied flows in coastal waters. Coast. Eng. 58 (10), 992–1012.